

*Università degli Studi di Pavia - Dipartimento di Scienze della Terra e dell' Ambiente*

DOTTORATO DI RICERCA IN SCIENZE DELLA TERRA E  
DELL'AMBIENTE

Fracture pattern and surface deformations induced by  
active buried faults: seismotectonic implications.

Yuri Panara

Academic Year 2019/20

Cycle XXXII

Coordinator:

Prof. Roberto Sacchi

Tutors:

Prof. Cesare Perotti

Prof. Silvio Seno

Prof. Giovanni Toscani



# Index

1. Introduction	1
1.1 References	7
2. Analogue models	10
2.1 Introductions	11
2.2 Material and scaling	13
2.3 Methods	16
2.3.1 <i>Experimental setup</i>	19
2.4 Result	30
2.4.1 <i>Maps/DEM.</i>	30
2.4.2 <i>Sections</i>	32
2.5 Discussion & Conclusions	34
References	36
Chapter 3. Numerical models	40
3.1. Introduction	41
3.1.1. Study Area	44
3.1.2. L'Aquila Seismic Sequence	46
3.2. Surface and Subsurface Data	46
3.2.1. Surface Data	47
3.2.2. Aftershock Data	49
3.3. Methodology	50
3.3.1. Fault Construction	50
3.3.2. Numerical Models	54
3.3.3. Line of Sight (LOS) Correction	55
3.4. Results	56
3.4.1. Residual Difference Maps	56
3.4.2. Median Net Difference	60
3.5. Discussion	61
3.6. Conclusions	67
References	68
Chapter 4. Slip inversion	75
4.1. Introduction	76
4.2. Methods	77

4.3 Results	81
4.4 Conclusions	83
4.5 References	84
5. General results & conclusions	89

# 1. Introduction

The occurrence of earthquakes is often related to the formation of areas of surface uplift or subsidence and to other surface evidence such as coseismic surface faulting or breaks, that are related to the geometry and kinematics of the deep seismogenic fault, and are possible to observe and measure using different techniques. The aim of this thesis is to investigate using analogue and numerical models the relationship among coseismic slip patches on normal fault and ground surface deformation (i.e. between the distribution of slip on the fault surface occurred during an earthquake and the pattern of coseismic surface uplift and subsidence). However, due to the absence of direct underground investigation (e.g. well log or seismic survey) the exact fault's geometry, shape and dimension are often unknown. Understanding how coseismic slip patch can propagate toward Earth surface is a topic of great interest for many fields of geological sciences (e.g. active tectonics, seismic hazard assessment, geomorphology and seismo-tectonics). Commonly, ground deformation is used to rebuild, through numerical models and algorithms, both the geometry and kinematic of the fault responsible for ground deformation. Normal faults develop laterally from 15-20 Km in Central Apennines (e.g Paganica fault see Vannoli et al., 2012 for a review) up to 40 km for the 1980 Irpinia earthquake (Amato and Selvaggi, 1993); independently of whether this faults are the dip usually vary in a range between 30-60° (Figure 1.1 and Jackson and White, 1989).

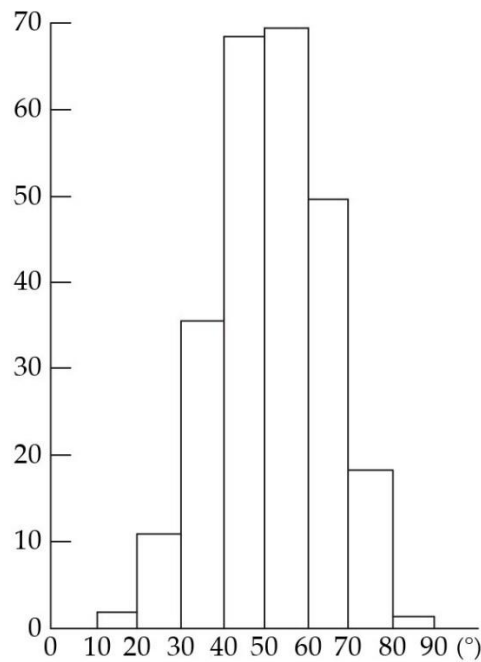


Figure 1.1. Dips of nodal planes for large ( $m_b > 5.2$ ) continental normal faulting earthquakes, measured from fault plane solutions. Faults from Greece, western Turkey, Italy, the Gulf of Suez, Tibet, NE China, SW China, Mongolia, East Africa, and the western U.S.A are included (modified after Jackson and White, 1989). Relationship between fault dip and host rocks lithology was not observed.

In the last twenty years, thanks to the development and implementation of new remote sensing techniques (e.g. DInSAR interferometry - Massonet et al., 1993; Atzori et al., 2009), new methods and tools has been developed to investigate this relationship. This approach has been developed also thanks to the recent improvement of satellite observations able to run automatic detection of fractures and/or diffuse deformations with precision, promising high resolution and high temporal frequency (Massonet et al., 1993). The implementation of these techniques is common in the study of seismic source, starting from surface deformation is possible to reconstruct the buried fault geometry at depth. New software and increased computing power enable fast and accurate data analysis. However, assumptions, uncertainties and hypotheses related to the geometry and kinematics of the faults remain consistent. In order to reconstruct the fault geometry, these geometric variables need to be previously defined among a limited set of options. We must therefore choose which parameters we want to investigate (e.g., dip, strike, length, width, position of

the upper tip, position of the lower tip, etc...). Despite that, inversion models usually provide single rectangular planar fault solution, this simplification may be excessive if the fault involved have a complex geometry or if there are multiple faults involved (e.g. Central Italy 2016 seismic sequence) (Lavecchia et al., 2016; Chiaraluce et al., 2017). Nevertheless, these new methods allow to rebuild fault geometries without any direct observation of the underground (e.g. seismic survey or well log). Often a study of structural geology is not possible to have direct information about the fault's configuration in depth. For this reason, simplifications are necessary; representing the faults as a rectangular and planar surfaces can be the best interpretation in many cases.

This thesis aims to investigate with a multidisciplinary approach the relationship occurring between the activity on normal faults and ground deformation. During the PhD we faced different aspect, the workflow was divided into three chapter:

1. We first run a wide number of analogue models in order to observe the contribution that different geometry parameter (such as fault size, dip, etc..) have on the final distribution of ground surface deformation. In this case, it was possible to observe the surface deformation knowing the exact geometry and depth of the fault. Hence, it was possible to quantify and constrain the contribution that single parameters have on final deformation;
2. After the first phase, we focused on a natural case. We first rebuild the geological model and later we used the interpreted fault geometries to obtain our numerical predictions. In order to validate the rebuild faults geometries we reproduced the observed DInSAR coseismic ground deformation observed after the April 6<sup>th</sup>, 2009 L'Aquila earthquake (Atzori et al., 2009). This simulation was run using Poly3D Boundary Element Method (B.E.M.) technique (Thomas, 1993). During this phase we also changed, the host rock stiffness and the stress drop using values proposed in literature, in order to make a sensitivity analysis on chosen parameters. By testing different fault geometries and two distinct rheological parameters we understood the importance that single constraints have on the final amount of surface deformation. In order to overtake the usual simplification of fault geometries we interpreted our

geological model using aftershock (Valoroso et al., 2013) and surface coseismic crack distribution (Emergeo Working Group 2009; Boncio et al., 2010). This method allows to rebuild, and lately use inside numerical models, non-planar faults geometries. The use of aftershock (and foreshock) distribution is particularly useful in seismic active areas like the Central Apennines where there isn't a direct knowledge of the deep geological setting (e.g. structural or stratigraphic settings) but there are several permanent or temporary seismic station network (e.g. Italian Seismic National Network) able to detect a very large number of seismic events. Moreover, in order to have a better constrain on horizontal component of the ground deformation, observed satellite deformation can be improved with GPS data obtained from geodetic station such as C.A.G.N (Central Apennines Geodetic Network) (Atzori et al., 2009).

3. For the last part, we try to reproduce the coseismic slip patch on the rebuild faults surfaces, the new clue is to use a non-planar fault geometry to run the inversion model. Fault geometries is a key factor in this kind of computation, having a non-planar reliable fault geometry can help to obtain more realistic and reliable slip distribution on fault surface. However, the results of these models are still preliminary.

Therefore, in this work we follow a multidisciplinary approach where we have alternated a theoretical method to the general problem (analogue modeling) with a direct investigation of the natural case (numerical and inversion models). For the natural case, we chose to investigate the well-know 2009 L'Aquila earthquake. L'Aquila seismic sequence was an ideal case of study having a long list of highly robust geological and geophysical data related with a recent seismic sequence. Both subsurface (e.g. aftershock and foreshock related with the main shock (Chiaraluce et al., 2009; Chiarabba et al., 2001; Valoroso et al., 2013) and surface data (e.g. DInSAR deformation, GPS data and surface cracks) were recorded, measured and published. Several reconstructions were proposed about the fault setting responsible for the April 6<sup>th</sup> mainshock (Boncio et al., 2010; Lavecchia et al., 2012; Bigi et la., 2013; Bonini et al., 2014; Castaldo et la., 2018; Panara et al., 2019; see Vannoli et



al., 2012 for a review); nevertheless, some remarkable issues persist about the fault's deep geometry. The proposed reconstruction mostly agrees about strike, dip and lower dip position describing the L'Aquila normal fault with a sub-planar surface; the main issues persist about the upper tip termination and about the possible reactivation of secondary faults surfaces. The L'Aquila (or Paganica) fault develops in an area of the Apennines currently under extension, but which was affected by compression during the formation of the mountain range. The thrusts that guided the mountain's uplift phase are no longer active but are still present in the area. It is reasonable to hypothesize that such mechanical discontinuities may play a role in the propagation of active normal faults. Unfortunately, the zone has never been investigated with sufficiently detailed seismic sections or sufficiently deep wells. For this reason, it is not possible to have a secure knowledge of the underground configuration. Main interpretation about L'Aquila fault are divided between blind, outcropping or blind fault interacting with an inherited low angle surface. In this thesis we have tried to analyze a wide range of possibilities and to observe which model best simulated the actual deformation observed after the mainshock of April 16, 2009.

This thesis has had the following results and conclusions:

1. A set of analogue models have been developed studying how surface deformation responds to changes in the main geometrical parameters of the fault;
2. Photogrammetry (a new, more accurate and precise methodology for the observation and analysis of analogue models) was used to observe and lately analyze the surface deformation. This methodology was successfully imported inside the Lab. Of Analogue Modeling of University of Pavia can be use in the future for other analogue experiment;
3. A wide series of numerical models have been developed in order to reproduce the observed coseismic deformation observed after the 2009 L'Aquila earthquake. A sensitivity analysis on three chosen parameters was performed in order to understand how surface deformation is affected by fault geometry, rock stiffness (Young's Modulus) and stress drop;

4. The numerical models result also help the better define the depth configuration of the fault responsible for L'Aquila seismic sequence suggesting the interaction between the main blind normal fault and a secondary, low-angle, shallower thrust fault.

## 1.1 References

1. Amato, A.; Selvaggi, G. Aftershock location and P-velocity structure in the epicentral region of the 1980 Irpinia earthquake. *Ann. Geophys.* 1993, 36.
2. Atzori, S.; Hunstad, I.; Chini, M.; Salvi, S.; Tolomei, C.; Bignami, C.; Stramondo, S.; Trasatti, E.; Antonioli, A.; Boschi, E. Finite fault inversion of DInSAR coseismic displacement of the 2009 L'Aquila earthquake (central Italy). *Geophys. Res. Lett.* 2009, 36.
3. Boncio, P.; Pizzi, A.; Brozzetti, F.; Pomposo, G.; Lavecchia, G.; Di Naccio, D.; Ferrarini, F. Coseismic ground deformation of the 6 April 2009 L'Aquila earthquake (central Italy,  $M_w > 6.3$ ). *Geophys. Res. Lett.* 2010, 37.
4. Bigi, S.; Casero, P.; Chiarabba, C.; Di Bucci, D. Contrasting surface active faults and deep seismogenic sources unveiled by the 2009 L'Aquila earthquake sequence (Italy). *Terra Nov.* 2013, 25, 21–29.
5. Bonini, L.; Di Bucci, D.; Toscani, G.; Seno, S.; Valensise, G. On the complexity of surface ruptures during normal faulting earthquakes: Excerpts from the 6 April 2009 L'Aquila (central Italy) earthquake ( $M_w 6.3$ ). *Solid Earth* 2014, 5, 389–408.
6. Castaldo, R.; de Nardis, R.; DeNovellis, V.; Ferrarini, F.; Lanari, R.; Lavecchia, G.; Pepe, S.; Solaro, G.; Tizzani, P. Coseismic Stress and Strain Field Changes Investigation Through 3-D Finite Element Modeling of DInSAR and GPS Measurements and Geological/Seismological Data: The L'Aquila (Italy) 2009 Earthquake Case Study. *J. Geophys. Res. Solid Earth* 2018, 123, 4193–4222.
7. Chiaraluce, L.; Valoroso, L.; Piccinini, D.; Di Stefano, R.; De Gori, P. The anatomy of the 2009 L'Aquila normal fault system (central Italy) imaged by high resolution foreshock and aftershock locations. *J. Geophys. Res. Solid Earth* 2011, 116.
8. Chiaraluce, L. Unravelling the complexity of Apenninic extensional fault systems: A review of the 2009 L'Aquila earthquake (Central Apennines, Italy). *J. Struct. Geol.* 2012, 42, 2–18.

9. Chiaraluce, L.; Di Stefano, R.; Tinti, E.; Scognamiglio, L.; Michele, M.; Casarotti, E.; Cattaneo, M.; De Gori, P.; Chiarabba, C.; Monachesi, G.; et al. The 2016 central Italy seismic sequence: A first look at the mainshocks, aftershocks, and source models. *Seismol. Res. Lett.* 2017, *88*, 757–771.
10. Chiarabba, C.; Amato, A.; Anselmi, M.; Baccheschi, P.; Bianchi, I.; Cattaneo, M.; Cecere, G.; Chiaraluce, L.; Ciaccio, M.G.; De Gori, P.; et al. The 2009 L'Aquila (central Italy)  $M_w$  6.3 earthquake: main shock and aftershocks. *Geophys. Res. Lett.* 2009, *36*.
11. Lavecchia, G.; Ferrarini, F.; Brozzetti, F.; Nardis, R. De; Boncio, P.; Chiaraluce, L. From surface geology to aftershock analysis: Constraints on the geometry of the L'Aquila 2009 seismogenic fault system. *Ital. J. Geosci.* 2012, *131*, 330–347.
12. Lavecchia, G.; Castaldo, R.; de Nardis, R.; De Novellis, V.; Ferrarini, F.; Pepe, S.; Brozzetti, F.; Solaro, G.; Cirillo, D.; Bonano, M.; et al. Ground deformation and source geometry of the 24 August 2016 Amatrice earthquake (Central Italy) investigated through analytical and numerical modeling of DInSAR measurements and structural-geological data. *Geophys. Res. Lett.* 2016, *43*, 12,389–12,398.
13. Massonnet, D.; Rossi, M.; Carmona, C.; Adragna, F.; Peltzer, G.; Feigl, K.; Rabaute, T. The displacement field of the Landers earthquake mapped by radar interferometry. *Nature* 1993, *364*, 138–142.
14. Panara; Toscani; Cooke; Seno; Perotti Coseismic Ground Deformation Reproduced through Numerical Modeling: A Parameter Sensitivity Analysis. *Geosciences* 2019, *9*, 370.
15. Thomas, A.L. Poly3D: A Three-dimensional, Polygonal Element, Displacement Discontinuity Boundary Element Computer Program with Applications to Fractures, Faults, and Cavities in the Earth's crust. Ph.D. Thesis, Stanford University, Stanford, CA, USA, June 1993.
16. Valoroso, L.; Chiaraluce, L.; Piccinini, D.; Di Stefano, R.; Schaff, D.; Waldhauser, F. Radiography of a normal fault system by 64,000 high-precision earthquake

locations: The 2009 L'Aquila (central Italy) case study. *J. Geophys. Res. Solid Earth* 2013, *118*, 1156–1176.

17. Vannoli, P.; Burrato, P.; Fracassi, U.; Valensise, G. A fresh look at the seismotectonics of the Abruzzi (Central Apennines) following the 6 April 2009 L'Aquila earthquake ( $M_w$  6.3). *Ital. J. Geosci.* 2012, *131*, 309–329.

## 2. Analogue models

In this chapter we describe how we run analogical models, how they were analyzed, and the main results obtained from them. Geoscientists have used analogue experimental models for more than a century to gain insight into the kinematic and dynamic evolution of geological structures (e.g., Cadell, 1889; Ramberg, 1981; Koyi, 1997). For all the experiment we focus on the reproduction of normal faults. Dry sand, a material extensively used in analogue models in structural geology studies, was employed in this series of experiments. The surface deformation of the models was analyzed using digital photogrammetry, in the analogue modeling laboratory of Pavia University structured light was previously used to detect the deformation. This technique allows to overcome some of the limits of the structured light because it increases the resolution of the observations and the automation of surfaces detection and analysis processes.

The purposes of the experiments were the study the variations of the surface deformations testing different normal fault geometrical parameters such as: width, depth and inclination. All the experiments were conducted using the same material (dry quartz sand) and keeping constant the boundary conditions of the experiments. These observations made possible to constrain the surface deformation pattern with the with known features of the buried fault.

## 2.1 Introductions

Extension in the upper brittle crust is mostly accommodated by faulting and fracturing. Understanding how these processes evolve over time and interact with the ground surface deformation is a topic of basic importance with numerous implications for geological sciences. Over time numerous analogue models have been proposed to analyze the behaviors of normal faults (McClay, 1990; Bonini et al., 2016). To better constrain the relationship between slip patch on fault surface and ground deformation it is important to constrain and understand how the fault geometry affects the surface deformation. This work can be interesting in order to quantify the importance that fault features (e.g. dip angle, fault size, fault area, etc.) have on the resulting surface deformation. The surface ground deformation is commonly the summation of different and separate processes. Although, the evolution and propagation of normal faults are affected by several parameters as the mechanical properties of the rock, geometry of the fault and tectonic setting in the area. Understanding the evolution over time and rebuilding the depth geometry are topics widely discussed in literature. One of the most common ways to rebuild fault geometry is observing the surface evidence such as cracks, fractures or slip surfaces on the ground. Three are the main parameters usually considered in this kind of studies: maximum displacement, total length of surface trace and the displacement distribution along fault trace (See Kim and Sanderson, 2005 for a review). The relationship between these features and spatial-temporal distribution have been investigated (Wells and Coppersmith, 1994), and they are often used to extract features that cannot be directly observed. For instance, maximum displacement along a fault is often used to estimate the magnitude of earthquakes through empirical formulas (Wells and Coppersmith, 1994; Biasi and Weldon, 2006). Nevertheless, it is necessary to remind how local lithological or geological heterogeneity (e.g. different fault systems) can complicate the system influencing the behavior and the propagation of the faults. Commonly in nature we have geological systems resulting from complex and multiple evolutionary stages, there may be a reversal of the tectonic style. During first development stages faults are usually confined in depth, only later they can propagate toward the Earth surface (Bürgmann et al., 1994). While an outcropping fault has clear surface evidence,

usually, blind fault's surface expressions are bending and folding or minor secondary fractures on topography. However, fault propagation can be diverted, slowed down or stopped by the interaction with pre-existing faults and fracture systems end/or with the interaction with lithological discontinuities because of changes in the mechanical and rheological properties (Bonini et al., 2015; Bonanno et al., 2017). All of these anisotropy deeply affect the behavior and evolution of faults systems and are usually observed together with superposition of different tectonic phases. Large-scale events affecting regional tectonics usually happen in correspondence of multiple extension phases (e.g. North Sea, African rift, Thailand) or when contractional regimes are followed by extensional tectonics (e.g. Alps and Apennines). At first, in such cases theoretical model cannot be accurate enough to rebuild the deep fault configuration. Another evidence associated with normal faulting inside Central Apennines is the presence of intramountain sedimentary basins (Bagnaia et al., 1992; Vezzani et al., 2009; Improta et al., 2012). These Apennine basins can have different sizes, they are usually shallow with modest sediment thickness compared to other intra-mountain basins (e.g. thickness up to few thousand meters were measured inside Basin-range in western north America) (Stewart, 1971; Stewart; 1978). Along the Apennines, they are characterized by depths from a few tens of meters up to a few hundred meters and filled with continental sediments (Improta et al., 2012). These basins are generally post-Messinian age and are superimposed upon the compressional Neogene structures (e.g. Fucino basin) (Cavinato and De Celles, 1999; Cavinato et al., 2002). Despite their limited size, they are numerous along a narrow area, about 400 km long and about 50 km wide, which grows within the central Apennines. Over the Apennines these basins are typically bordered by high-angle normal faults active over Quaternary. There is therefore a direct relationship (geometric and genetic) between position, size and shape of these basins and the fault that formed them. However, the basins we observe today in the Central Apennines are the result of a long geological process. The fault, or the fault system, which causes its formation undergoes several reactivations over time. Different earthquakes can also cause the reactivation of different sectors of the same fault. The basins we observe are the summation of several seismic sequence, this summation is what we want to analyze in



this chapter. Instead, after each seismic sequence a slight deformation is observed on the ground. This deformation is typically between a few decimeters (e.g. L'Aquila earthquake -28 cm, Central Italy seismic sequence -20 Cm) in the Apennines (Atzori et al., 2009). This deformation is the direct result of a single geological event, but it is not possible to reconstruct it by observing the geometry of an entire intramountain basin. In this chapter the relationship between the faults geometry and the ground deformation has been investigated through analogue models. In particular, we focused our attention on understanding the role-played geometrical fault's features. In the attempt of clarify how fault effect the surface deformation pattern we considered the following properties: dip angle, burial depth and fault width. For all the experiment total extension and material rheology (quartz dry sand) have been kept constant.

## 2.2 Material and scaling

Because of their versatility and ease of execution (fast and cheap) analogue models are a very popular tool for investigations in structural geology studies. Using this approach is possible to reproduce, observe and understand also the behavior of upper rigid crust. However, only few materials are considered reliable to scale a reliable model. The most common are wet clay (e.g. Cooke et al., 2012; Cooke et al., 2013) and dry sand (e.g. Bonini et al., 2006). According to several studies both are reliable for this analysis. Still today, dry granular materials are the most used for analogue experiment and it is also possible to investigate the deformation inside the sand volume. Using water or gelatin it is possible to consolidate the analogue experiment and observe the internal deformation.

Nevertheless, every laboratory uses different approach and materials, this made difficult to make quantitative comparison between similar experiment (Schreur et al., 2006). Main differences between similar models are mostly related with:

- boundary conditions, such as models' widths and length or base and sidewalk friction (Schreur et al., 2006);
- location of the observations, e.g. top view versus side view;
- materials properties: for example, we can choose clay, dry sand or glass microsphere changing also grain size and shape (Shellart, 2000). It is possible to pre-cut the clay to

simulate a pre-existing discontinuity (Cooke et al, 2013; Bonanno et al., 2017) or simulate a homogeneous material without discontinuities;

- differences in the experiment set up, for example there are different techniques available to detect surface or internal deformation. It is possible to measure the deformation by structured light, laser scanner or digital imaginary methods (see Graveleau et al., 2012 for a review).

However, analogue models represents an incredible tool allowing reproduction and direct observation of long-time scale geological processes. Usually analogue models are executed in normal gravity conditions. Important differences between different materials persist on density, frictional properties, grain size and shape. Several laboratories measured the frictional properties of their granular materials using either a Hubbert-type shear box (Hubbert, 1951), a ring-shear tester (Schulze, 1994) or a Casagrande shear box (Casagrande, 1932). Mean ring-shear error is usually smaller than 1% (Schreur, 2006). Analogue modelers usually assume that brittle materials deform according to Coulomb failure criterion with constant frictional properties. However, numerous studies demonstrate that materials such as quartz sand, corundum sand and glass microbeads are characterized by elastic/frictional plastic behavior with strain-hardening preceding failure and subsequent strain-softening until a stable value is reached (Schreur, 2006; Lohrmann et al. 2003; Panien 2004). This behavior is close with the observations on rocks deformed during experiment (Schreur et al., 2006; Marone 1998; Barnhoorn et al. 2004). Internal friction angle for quartz sand is between  $33^\circ$  and  $45^\circ$  (Table 2.1), this range of value is comparable with the one determined for rocks in the upper crust (Byerlee, 1978).

Table 2.1. Quartz sand properties and grain characteristics used in different laboratories (Schreur et al., 2006). Schreur et al., 2006 made a comparison between the same experiment run in different laboratories with very similar setup, materials and boundary condition. Even in this ideal situation it was possible to detect notable differences in the results.

Laboratory (Town)	Density ( $\frac{Kg}{m^3}$ )	C at $\phi$ peak ( $^\circ$ )	$\Phi$ peak ( $^\circ$ )	Strain soft. (%)	Grain size ( $\mu m$ )	Grain shape	Composition (%)
Bern	1560	21+18	35.5	15	80-200	Angular	99% SiO <sub>2</sub>
Florence	1550	66	39	n.d.	<250	Rounded	n.d.
Kyoto	1390	n.d.	n.d.	9	m = 203	Angular	93% SiO <sub>2</sub>
Parma	1500	n.d.	34.1	n.d.	60-250	Sub- rounded	99.8% SiO <sub>2</sub>
Pavia	1500	n.d.	33.2	4.1	60-250	Ang. to sub.ang	99.8% SiO <sub>2</sub>
GFZ Pozdam	1740	94 $\pm$ 7	35.4 $\pm$ 0.3	20.2	20-230	Weel- rounded	95% SiO <sub>2</sub>
IFP Rueil- Malmaison	1500	n.d.	45	39	m=116	Angular	>98% SiO <sub>2</sub>
Toronto	1625	3	35.7	29.2	150-200	Angular	<98% SiO <sub>2</sub>
Upsala	1350	150	33	30	60-250	Angular	97% SiO <sub>2</sub>

Scaling between analogue models and upper-crust condition can be achieved by observing kinematics, geometric and dynamic similarity (Hubbert, 1937). We assumed that 1 Cm in our analogue models corresponded to 1 Km inside the upper crust, we also assumed that angle of internal friction is the same in both cases (Schreur, 2006). In the equation 1 we have that:

$$\frac{C_p}{p_p} = 10^{10} \frac{C_m}{p_m} \quad (1)$$

C is cohesion and  $p$  is density.  $p$  is referred to natural condition while  $m$  is for analogue models' condition. Considering  $p_p$  equal to 1600 kg/m<sup>3</sup> and  $p_m$  equal to 2800 kg/m<sup>3</sup>, a cohesion of 10 Pa in the model corresponds approximately to 2 MPa in nature. Using dry

sand, after an extension of 1 Cm is typically possible to see fault expression on the surface. This means that fault propagation on sand surface is extremely fast, it hard to observe the progressive fault outcropping on the experiment surface. Wet clay allows a better observation of these phenomena (Cooke et al., 2012; Cooke et al., 2013) however it doesn't allow to observe the internal deformation. Another key factor to considered during extensional experiment is the width of the sandbox. In such experiment, where the width is perpendicular to the extension, lateral friction has a great importance influencing the fault position, number and evolution in the narrow models. For this reason, we decide to keep sandbox wider than other experiment (Schreur et al., 2006) and use graphite powder to reduce the grip. Together with materials properties, wall properties, differences in the location of the observation, box with a variable able to affect the resulting deformation. For ours model we used a 200  $\mu\text{m}$  quartz sand, see table 2.1.

## 2.3 Methods

Modeling of geological processes started back as the beginning of the 19th century with the simulation of compressive tectonic regimes (Gorceix, 1924; Paulcke, 1912; Summers, 1933). These analogue models, although very simple, allowed to reproduce remarkable structures. Even the first experiments mainly used sand, clay or alternations between the two materials; but it was not clear what the best properties were (e.g. grain size, layer thickness, clay water content, etc.). From their observation and their study, the main rheological properties were soon derived. With the refinement of these techniques, the models started to be scaled adequately. Within a few years, numerous other experiments were conducted to reproduce the various disparate tectonic settings. Despite the rapid progress the experiments were always operated manually with a piston. Furthermore, deformation observations were limited to a qualitative approach. Although it is an ancient technique, analogue modeling has experienced an improvement in recent decades. With the arrival of the computer it was possible to calibrate with precision the direction, intensity and speed of the deformation thanks to the use of computer controlled motorized pistons. But it was in the observation methodologies that the technique was more improved. As already mentioned, the way in which the experiment is observed is as important as the

experiment itself. It is possible to observe the experiment from different point of view and make observations inside the experiment by cutting (to observe internal deformation when the experiment is finished). For this set of experiments, we have chosen to observe mainly the surface deformation. There are techniques for this observation, each with its own characteristics, advantages and disadvantages.

Nevertheless, having a reliable method to detect the model's deformation (internal or external) is a key factor to make the results reliable. Typically, analogue models' laboratories can use a wide range of techniques to detect the deformation. The most common are:

- Structured light, a technique able to record 3D subsidence/uplift pattern along the fault systems projecting a known light pattern on the surface. The light pattern is often composed by horizontal/ vertical parallel bars. The device is typically formed by a projector while the deformation is measured by one or two cameras. The system provides mesh surface (usually .obj file) with the spatial space orientation of the cameras, for any further analysis or measurement the orientation needs to be fixed inside a different work environment (e.g. Move© software).
- Digital Image Correlation (DIC) method, an optical technique in visible light which aim the detection of particle movement using subsequent pictures taken for every step of deformation during the analogues model. In order to help this recognition, can be beneficial to spread colored particles over the model's surface. All the figures are fixed inside the same reference system. With this technique it is possible to quantify displacement and strain field. We used PIVlab software (Thielicke, 2014; Thielicke and Stamhuis, 2014);
- Digital Photogrammetry, a sensing digital technique which allow to rebuild 3D information. In geology is typically applied for rebuild outcrops (Menegoni et al 2018; Menegoni et al., 2018).

Other methods as CT scan or laser scanners provide different result, with the first one is possible to detect the internal deformation during the experiment with the secondo one is possible to achieve very high-resolution results (Galland et al., 2012). However, the cost is usually higher and the obtained results do not necessarily justify the charge. We decided to

use digital photogrammetry instead of structured light until then used in the Laboratory of Analogue modeling of Pavia. Although it requires more effort than structured light (longer working times, longer results processing times) it guarantees greater versatility and greater precision. The main advantage we mention now is that while structured light provides a single .obj file, digital photogrammetry allows different types of files to be obtained by controlling resolution, size and reference system. This precision and versatility also affect the subsequent processing phase when it is then possible to obtain more precise and reliable observations on the deformations observed.

### 2.3.1 Experimental setup

The aim of our analogue experiment was to study the relationship between a single normal fault inside the upper brittle crust and surface deformation. For this reason, we varied the thickness of the sandbox between 10 and 8 Cm. In this way we simulate the first 8-10 km of natural system. The sandbox was 70 Cm long, 40 Cm wide (Figure 2.1), the sand thickness varies with the different experiments

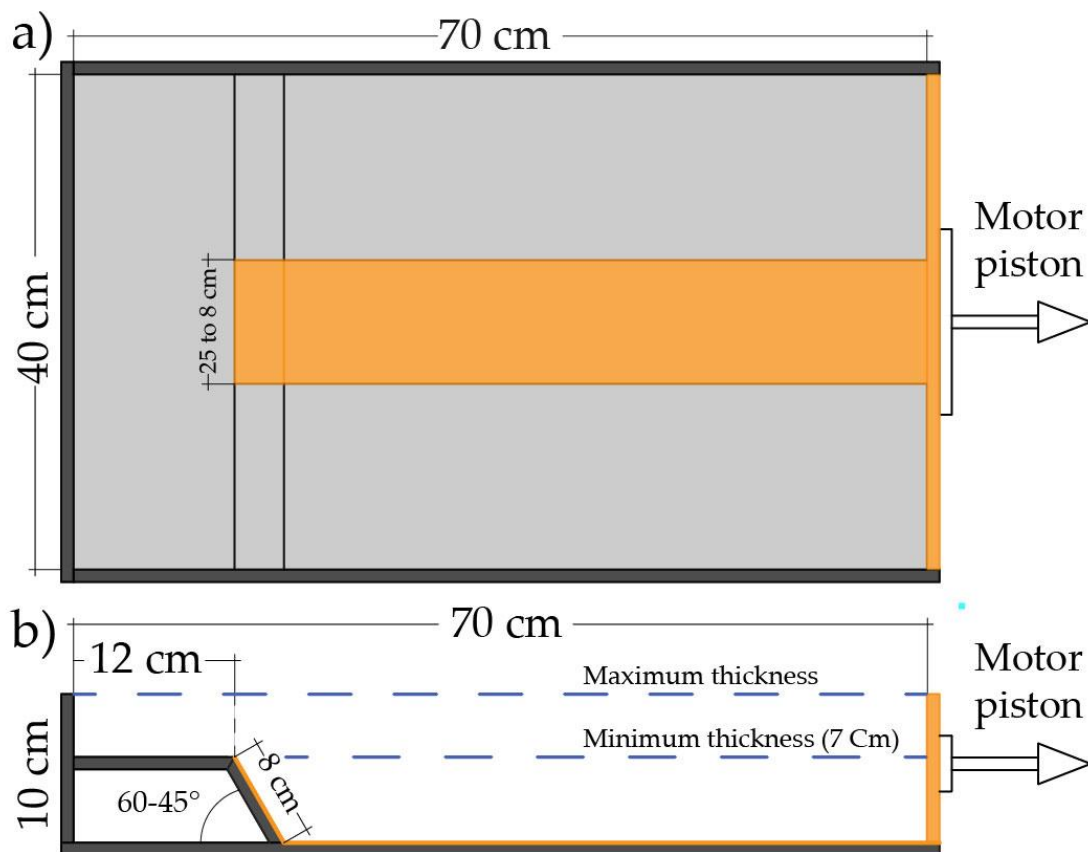


Figure 2.1. General setup of the analogue experiment in (a) top and (b) section view. Notice the position of the motor piston and the moving strip providing deformation in the system.

The base of the sandbox has a ramp-flat-ramp geometry, the upper ramp was 10 cm while the lower ramp was 60 cm long. Two different ramp dip has been tested, 45° and 60° in order to test the end members of the average dip value commonly measured for normal faults (Jackson and White, 1989). We also tested different fault width and sand thickness. The parameter chosen for each experiment are summarized in Table 2.1.

Table 2.1. This table summarize the different parameters tested for each analogue models.

Model	Tot. extension	Fault Dip	Fault Width	Depth
Model 1	11.5 mm	45°	25 cm	3.0 cm
Model 2	11.5 mm	45°	25 cm	""
Model 6	11.5 mm	45°	25 cm	0.0 cm
Model 4	11.5 mm	45°	25 cm	7.0 cm
Model 5	11.5 mm	45°	25 cm	1.0 cm
Model 6	11.5 mm	45°	25 cm	4.5 cm
Model 7	11.5 mm	60°	25 cm	0.0 cm
Model 8	11.5 mm	60	25 cm	1.0 cm
Model 9	11.5 mm	60	25 cm	3.0 cm
Model 10	11.5 mm	60	25 cm	4.5 cm
Model 11	5.0 mm	60	25 cm	4.5 cm
Model 12	11.5 mm	60	25 cm	4.5 cm
Model 13	8.0 mm	60	25 cm	4.5 cm
Model 14	11.5 mm	60	25 cm	4.5 cm
Model 15	11.5 mm	60	8 cm	4.5 cm
Model 16	11.5 mm	60	12 cm	4.5 cm
Model 17	11.5 mm	60	16 cm	4.5 cm
Model 18	11.5 mm	60	20 cm	4.5 cm
Model 19	11.5 mm	60	4 cm	4.5 cm
Model 20	11.5 mm	60	24 cm	4.5 cm

Total extensional deformation of 20 mm has been imposed to the basal strip in steps of 1 mm by a computer-controlled motorized piston. We build two separate sandbox in order to cover a wide range of possible cases.



### *2.3.2 Structure from motion Photogrammetry*

Restoring and accurately mapping the deformation of an analog model is a procedure of fundamental importance. Over the years different techniques have been used to map this deformation. The Pavia laboratory is equipped with a structured light device, which is not always able to carefully reconstruct the deformed experiment's surface. Among the advantages of this set-up we can mention the great versatility of use and the great speed in the processing of the results. However, this methodology has some limitations, the two most relevant are: the inability to reconstruct the surface of the model in the shaded areas and the inability to reconstruct the surface on opaque materials such as glass. Other instruments, like laser scanners, do not present these problems and are able to guarantee the maximum precision of the result in every possible condition. However, this type of instrumentation has a considerable expensive and requires constant maintenance.

During this PhD we wanted to try a new technique for observing the surfaces of analog models by applying the Structure from Motion (SfM) technique. This technique, born in the 90s, allows the three-dimensional reconstruction of objects at various scales (Spetsakis and Aloimonos, 1991). SfM technique use several 2D RGB pictures, from 10s to 100s to rebuild, to recognizing homologous pixel on two or more images (Figure 2.2).

These pixels are used to recreate a 3D surface model through a bundle adjustment process reconstructing the images orientation and minimizing the residual errors (Bemis et al., 2014). Sturznegger and Stead (2009) define three main steps to be defined before a the photogrammetry survey; (1) specify the resolution necessary to achieve for the survey (e.g. millimeter, centimeters, etc.), (2) define camera's parameters such as resolution and camera-subject distance (camera outcrop usually, camera-sandbox in this studies), and ultimately (3) define the area to study in order to prevent problems on the final result such as area (e.g. hidden

area  
were  
the

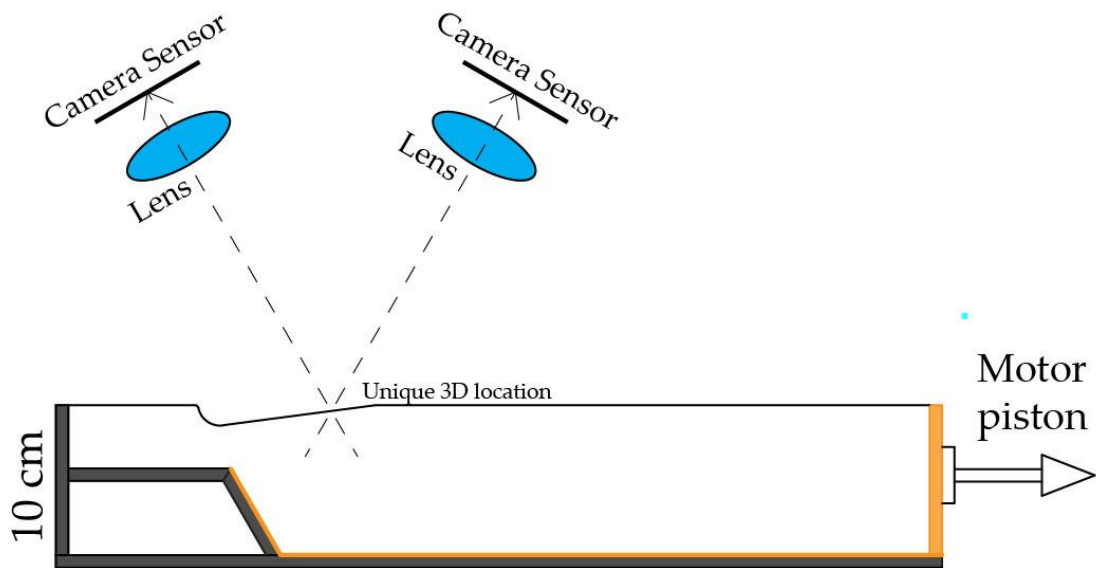


Figure 2.2. Schematic representation of how photogrammetry works.

deformation was mostly focused). About the last point (3), a typical problem using structured light is that in the area where the deformation is sharp, hidden areas can be observed. On this portion of the surface it is impossible to accurately record the deformation, digital photogrammetry allows to overcome this problem permitting to entirely rebuild a consistent surface. The distance between camera (or cameras) and the subject is remarkably important to determine the final resolution of the photogrammetry. The resolution was defined by Birch (2006) as:

$$\text{Ground Pixel Size [m/pixel]} = \frac{\text{Distance (Camera subject) [m]}}{\text{Focal length [m]}} * \text{Pixel size (camera) [m/pixel]} \quad (2)$$

For these photogrammetry survey we used a Canon 600D 24 MPixel. Starting from a dataset of pictures from different angles of the object to be reconstructed, the software recognizes the common pixel form different figures thus reconstructing the 3D object and orienting the images in space. The advised overlap between individual images is from 60 up to 80% of the figure. Higher overlap guarantees a better resolution on the final dense cloud. Nowadays different software allows to create 3D models with this technique, VisualSfM (Wu et al., 2011; Wu, 2013) and MicMac (Rupnik et al., 2017) are open source while Agisoft Photoscan© and Pix4D© are commercial software's. All these have different feature, but they all share two specific procedures. They all match the figures using Scale-Invariant Feature Transform (SIFT) algorithm (Lowe, 1999; Lowe, 2004). The second common process is the performing of the Bundle Adjustment process (B.A.) in order to recreate a point cloud. This technique has been extensively applied in geology for studies related with the analysis of rocky outcrops (Menegoni et al., 2018, Menegoni et al., 2019). However, the method requires a reference system that helps to quantify the error. Also structured light technique allow an error estimation, however, to calibrate the reference system with photogrammetry is much faster procedure. For drone photogrammetry GPS information are used to calibrate the reference system. For our model we have created a local reference system composed of 55 markers arranged along the edge of the sandbox. These markers were arranged along the three axes X, Y and Z, this helps to obtain a more accurate result. The images were all taken with the same machine in the same lighting conditions. Each image has included all the sandbox and all the markers from different angles, the redundancy of the same subject helps to increase the quality of the final result by increasing the quality of BA process (Francioni et al., 2017) and excluding blurry pictures from the models (Turner et al., 2014).

Table 2.2. Average value of the parameter considered for the photogrammetry.

Camera Numb.	Resolution	G.C.P. <sup>1</sup>	Error	Tie points
70-110	0.15 mm/pixel	55	~0.30 mm	~130.000

1 G.C.P. Ground Control Point.

For this research we used Photoscan (Agisoft®), a software widely used in photogrammetric reconstructions (Menegoni et al., 2018; Menegoni et al., 2019). The procedures the software used to run the Sfm reconstruction is summarized in Lucieer et al., (2013) and Turner et al., (2014) as follows: (a) the pictures are preprocessed in order to be georeferenced, (b) the image were matched and aligned (with the highest precision allowed by the software) in order to rebuild a sparse point cloud. This sparse cloud was typically composed by few hundred thousand point; (c) then a dense points cloud was created. This cloud had typically a  $10^6$  points, to get the next steps of the routine faster and to achieve a better result, the points out of the sandbox surface (e.g. sandbox wall or motor piston) were removed. (d) Starting from the information contained inside the dense point cloud a mesh surface was created using the best option quality provided by the software. The sandbox has a size of 70X40 cm, with a total area of 2,800 cm<sup>2</sup>.  $10^6$  points on such small area involves a very high point density, around 420 points per cm<sup>2</sup>. If the reference system is robust, this point density allows to rebuild experiment surface with very high precision detecting minimum deformations.

Ultimately, Agisoft® also allow to create a (e) .tiff format orthophoto mosaic. For this experimental set-up a typical Agisoft® contained around 80 pictures inside, to run all the steps we just listed several hours were necessary. The great computation time is the most significant problem related with the photogrammetry technique. However, it was made possible to program an automated workflow routine using Python, an high-level general-purpose programming language (Van Rossum, 1991).

The procedure was divided into four separated cycles, once defined a common file path Python® can automatically import the input data and export and save, in the prescribed folders and file format, the results. The only procedures we were not able to implement inside the cycles are, the creation of Photoscan® file, the upload of the pictures and the resize of the model region. The resize of the region need to be done at the end of cycle 1, we decide to keep cycle 2, 3 and 4 separated in order to have a better control on

results. With these Python script it is also possible to fully define the setting parameter such as: precisions, tolerance, file format, pixel size.

Cycle 1; run the pictures alignment and save the results.

```
import PhotoScan
doc = PhotoScan.app.document

percorso=r"C:/ciclo/step_agisoft"

dem=r"C:/ciclo/dem/dem_"
orto=r"C:/ciclo/ortofoto/ortofoto_"
punti=r"C:/ciclo/dense_cloud/dc_"
report=r"C:/ciclo/report/report_"

lista=[f for f in os.listdir(percorso) if ".psx" in f]

for l in lista:
    doc.open(os.path.join(percorso,l))
    chunk = doc.chunk
    chunk.detectMarkers(type=PhotoScan.TargetType.CircularTarget12bit,
tolerance=70, inverted=False, noparity=False)
    chunk.crs = PhotoScan.CoordinateSystem('LOCAL_CS["Local
CS",LOCAL_DATUM["Local Datum",0],UNIT["metre",1]]')
    # ppcoor = PhotoScan.app.getOpenFileName("")
    ppcoor = ("C:/ciclo/Marker_positions.csv")
    if ppcoor[-4:].lower() == ".csv":
        refform = "csv"
    else:
        PhotoScan.app.messageBox("no .csv data selected")
    chunk.markers[0]=chunk.loadReference(ppcoor,format = refform, columns=
'nxyz', delimiter=';')
```

```

        chunk.updateTransform()
        chunk.matchPhotos(accuracy=PhotoScan.HighAccuracy,
preselection=PhotoScan.GenericPreselection,          filter_mask=False,
keypoint_limit=40000, tiepoint_limit=40000)
        chunk.alignCameras()
        chunk.optimizeCameras(fit_f=True, fit_cxcy=True, fit_b1=True, fit_b2=True,
fit_k1k2k3=True, fit_p1p2=True, fit_k4=True, fit_p3=False, fit_p4=False)
        doc.save()
doc.save()

```

Cycle2: run the optimization of the cameras, build the dense cloud, model and the texture.

```

import os
import PhotoScan
doc = PhotoScan.app.document

percorso=r"C:/ciclo/step_agisoft"

dem=r"C:/ciclo/dem/dem_"
orto=r"C:/ciclo/ortofoto/ortofoto_"
punti=r"C:/ciclo/dense_cloud/dc_"
report=r"C:/ciclo/report/report_"

lista=[f for f in os.listdir(percorso) if ".psx" in f]

for l in lista:
    doc.open(os.path.join(percorso,l))
    chunk = doc.chunk
    chunk.optimizeCameras(fit_f=True, fit_cxcy=True, fit_b1=True, fit_b2=True,
fit_k1k2k3=True, fit_p1p2=True, fit_k4=True, fit_p3=False, fit_p4=False)

```

```
doc.save()
chunk.buildDenseCloud(quality=PhotoScan.MediumQuality)
doc.save()
chunk.buildModel(surface=PhotoScan.Arbitrary,
interpolation=PhotoScan.EnabledInterpolation, face_count=1000000)
doc.save()
chunk.buildUV(mapping=PhotoScan.GenericMapping, count = 4)
doc.save()
chunk.buildTexture(blending=PhotoScan.MosaicBlending, size=4096)
doc.save()

doc.save()
```

Cycle 3: created and save a D.E.M., orthophoto, dense cloud (the same created in cycle 2) and a report of the model.

```
import os
import PhotoScan

doc = PhotoScan.app.document

percorso=r"C:/ciclo/step_agisoft"

dem=r"C:\ciclo\dem"
orto=r"C:\ciclo\ortofoto"
punti=r"C:\ciclo\dense_cloud"
report=r"C:\ciclo\report"
obj=r"C:\ciclo\obj"
```

```

lista=[f for f in os.listdir(percorso) if ".psx" in f]
for l in lista:
    doc.open(os.path.join(percorso,l))
    chunk = doc.chunk
    chunk.buildDem(source=PhotoScan.DenseCloudData,
interpolation=PhotoScan.EnabledInterpolation)
    chunk.buildOrthomosaic(surface=PhotoScan.ElevationData,
blending=PhotoScan.MosaicBlending,    color_correction=False,    dx=0.147898,
dy=0.147898)

    sublist=l[0:-4]
    chunk.exportDem(os.path.join(dem,sublist+".tif"), format="tif", dx=0.5, dy=0.5,
nodata=-32767, write_kml=False, write_world=False, tiff_big=False)
    chunk.exportOrthomosaic(os.path.join(orto,sublist+".tif"),    format="tif",
raster_transform=PhotoScan.RasterTransformNone,    dx=0.14,    dy=0.14,
write_kml=False, write_world=False, tiff_compression="lzw", tiff_big=False)

    chunk.exportPoints(os.path.join(punti,sublist+".xyz"),
source=PhotoScan.DenseCloudData,    precision=6,    normals=True,    colors=True,
format="xyz" )
    chunk.exportModel(os.path.join(obj,sublist+".obj"))
    chunk.exportReport(os.path.join(report,sublist+".pdf"))
doc.save()

```

Cycle 4: created and export D.E.M. and orthophoto cut around the area off maximum deformation in order to minimize the boundary effect that can occur in the edges of the model (problem caused by a lower pictures coverage on the edge). These D.E.M. surface are the one we used in the data analysis.

```
import os
```



```

import PhotoScan

doc = PhotoScan.app.document

percorso=r"C:/ciclo/step_agisoft"

dem_tagliato=r"C:\ciclo\dem_tagliato"
orto_tagliata=r"C:\ciclo\ortofoto_tagliate"

lista=[f for f in os.listdir(percorso) if ".psx" in f]

for l in lista:
    doc.open(os.path.join(percorso,l))
    chunk = doc.chunk
    chunk.buildDem(source=PhotoScan.DenseCloudData,
interpolation=PhotoScan.EnabledInterpolation, region=(40, 240, 390, 480))
    chunk.buildOrthomosaic(surface=PhotoScan.ElevationData,
blending=PhotoScan.MosaicBlending, color_correction=False, region=(50, 240, 390, 450),
dx=0.147898, dy=0.147898)

    sublist=l[0:-4]
    chunk.exportDem(os.path.join(dem_tagliato,sublist+".tif"), format="tif", region=(50,
240, 390, 450), dx=0.5, dy=0.5, nodata=-32767, write_kml=False, write_world=False,
tiff_big=False)
    chunk.exportOrthomosaic(os.path.join(orto_tagliata,sublist+".tif"), format="tif",
raster_transform=PhotoScan.RasterTransformNone, region=(50, 240, 390, 450), dx=0.14,
dy=0.14, write_kml=False, write_world=False, tiff_compression="lzw", tiff_big=False)

doc.save()

```

Using this procedure, it was possible to rebuild a large number of deformation surfaces, using a standard automatic procedures. The data collected were analyzed in order to observe and describe the deformation pattern on analogue experiment.

## 2.4 Result

In this chapter we are going to show the most significant result collect from analogues models. We are going to show maps of total deformation and cross section showing the internal deformation after the experiment. We chose six model within the twenty we run, all the select models have a  $60^\circ$  dip angle, while we made vary the other parameters (Table 2.3).

Table 2.3. Geometrical features chosen for the analogue experiment.

Experiment	( $^\circ$ )	Extension (mm)	Fault depth (mm)	Fault width (mm)
a)	60	11.5	10	250
b)	60	11.5	30	250
c)	60	11.5	45	250
d)	60	5.0	45	250
e)	60	11.5	45	200
f)	60	8.0	45	250

### 2.4.1 Maps/DEM.

We represent the final deformation by creating maps of the difference, this plot was made comparing the initial surface with the final one after the extension. Color scale is the same for all the maps in order to compare the results. We keep constant box dimension, quartz sand, dip angle and direction of the extension. The deformation was divided inside 0.5 mm steps and was not run in a single time. The extension was imposed with a motorized piston. Speed and acceleration were 0.1 mm/s and  $0.1 \text{ mm/s}^2$  respectively. For all the experiment the main fault has reached the surface after few millimeters of extension.

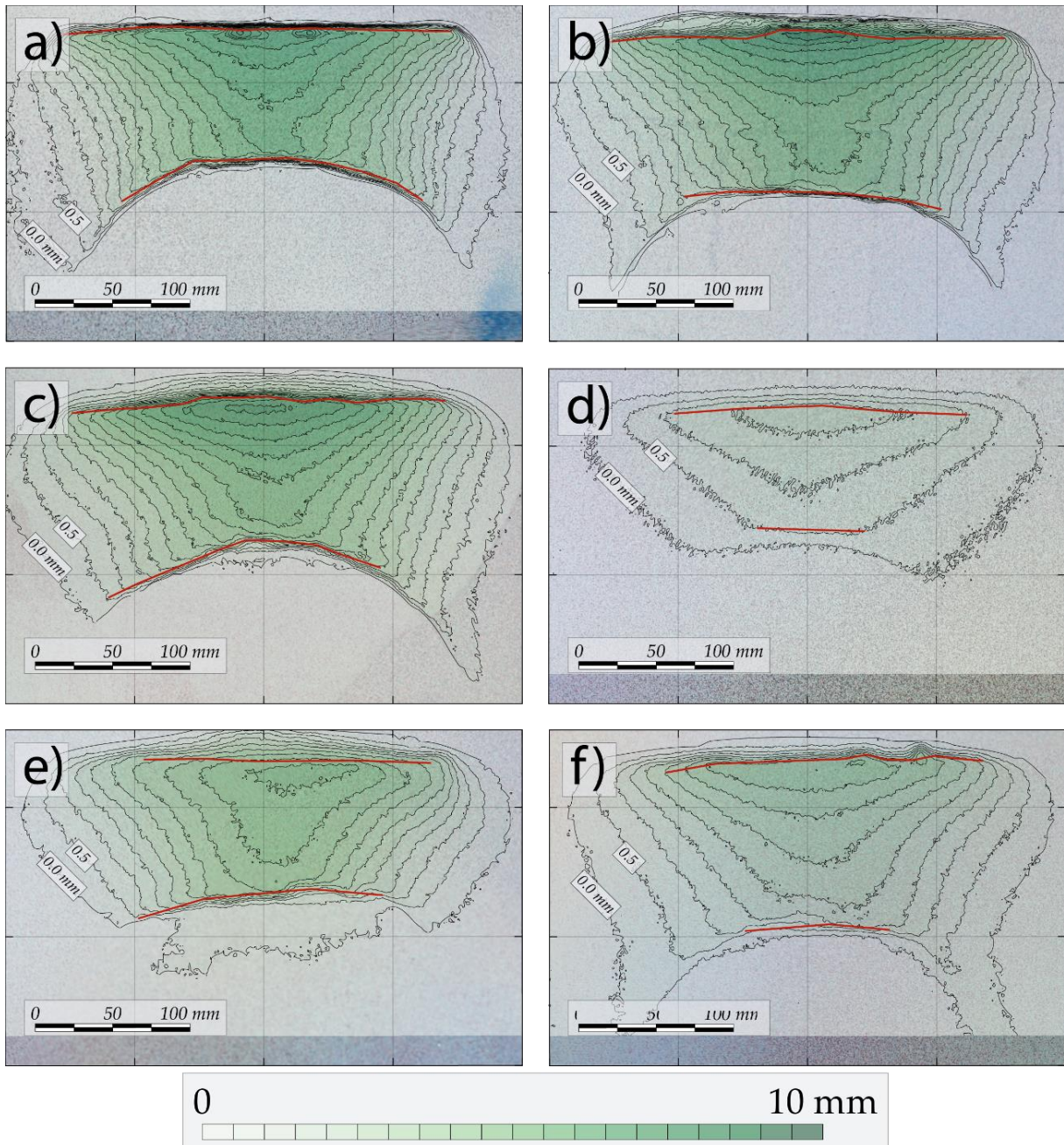


Figure 2.3. Maps showing the total deformation, they were obtained by comparing the initial surface with the final one at the end of the experiment. Extension is toward south. Red lines represent fault observed on sand surfaces.

Observing the detected deformation, it is possible to notice some common features. Red lines represent for all the experiment the outcropping faults. Using quartz sand, it is possible to observe fault propagation at surface after few millimeters of extension. The faults placed in northern area represent the propagation of the main fault, while the fault place in the southern area in the experiment represent the antithetic structures. The main faults cut the

surface before the secondary one, they are longer and better exposed. The antithetic structures also show a curvature related with the experimental setup, the paper drive a transcurrent deformation under the sand. This was intended to clearly highlight the deformation trend. In the first phases, on the other hand, the observed deformation was entirely comparable to the one observed in real cases. That is, a sub-ellipsoid deformation with the depocenter biased towards the upper tip of the fault.

### 2.4.2 Sections

At the end of the experiments all the analogue models were sliced in order to observe the internal deformation. During the experimental setup black horizontal layer were spread inside the quartz sand volume. This layers were also rebuilt with photogrammetry in order to have an accurate constrain on their position. After the experiment a thick layer of colored sand was spread above the experiment surface. This procedure was made necessary to saturate the experiment with water, so that was possible to cut the experiments. We cut the sections every 5 cm in order to observe the lateral evolution of the deformation. Observing the central section (Figure 2.4) we notice some remarkable feature.

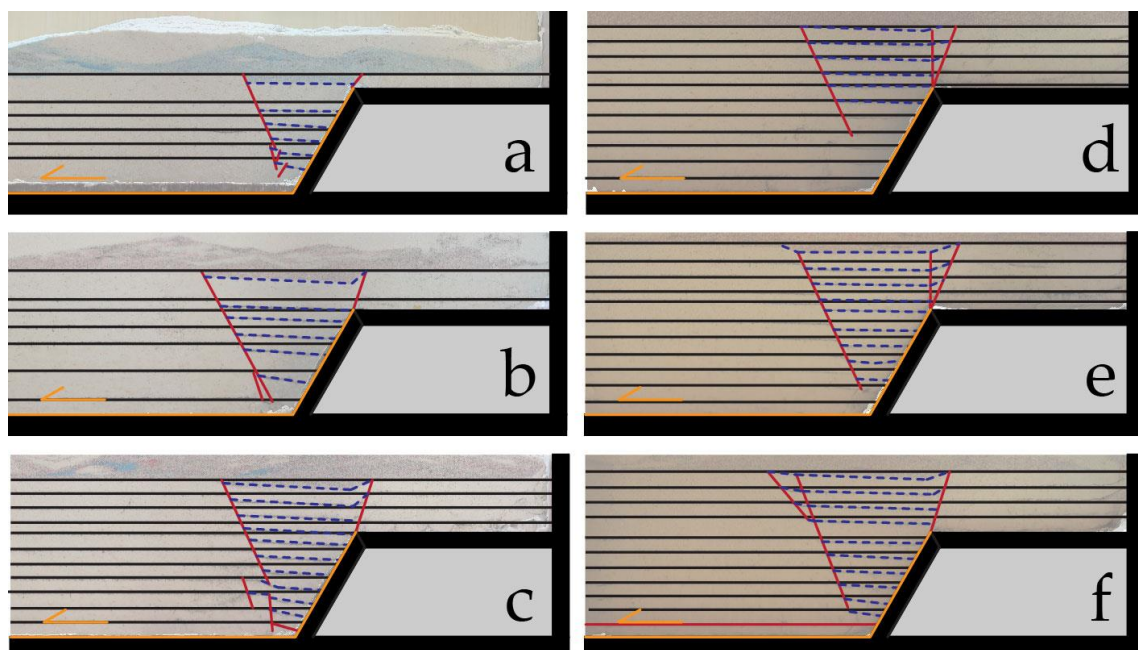


Figure 2.4. Orthophotos showing the internal deformation after the extension. Blue lines represent the deformed horizons, black line represent the undeformed situation, red line represent the faults inside sand volume. Orange line represent the paper strip.

All the selected experiments have a  $60^\circ$  dip, orange line shows the moving strip. The black horizons show the undeformed situation. While the blue lines show the deformed horizons. The observed faults are marked in red. It is possible to see how the main fault spreads directly to the surface. The upward dip angle of inclination of the propagation of the fault is slightly higher than the  $60^\circ$  of the main fault. The antithetic fault develops independently, without any imposition. The angle of inclination is very similar to that of the main fault, around  $60^\circ$ . In addition to the two most important faults, a series of secondary faults are observed. These secondary faults accommodate deformation at depth. However, these structures do not appear to significantly affect the observed ground deformation. In the event that the fault was at 45 degrees a different phenomenon was observed. The antithetic fault developed in a similar manner with an angle of about  $60^\circ$ . however, the main fault did not follow the pre-set  $45^\circ$  angle, but developed independently at an angle of about  $60^\circ$  for the experiments conducted. The deformation tends to reduce laterally in a very rapidly. Outside the fault width set in the experiment it is almost totally absent. Within the sand volume, the transcurrent structures observed on the surface have never been clearly observed. Despite the normal faults beginning to develop clearly from the first phases of the extension, the structures that flow past are generated later.

## 2.5 Discussion & Conclusions

With these analog models it has been possible to observe how surface deformation evolves within a well-constrained system. We simulated the propagation of a normal fault by varying 3 geometrical parameters: burial depth of the upper tip, inclination and width of the fault. We have observed how the deformation is sensitive to the chosen parameters. In particular, we have observed how the maximum depth of the depocenter is related to the burial depth of the upper tip of the fault (Table 2.4).

Table 2.4. Geometrical features chosen for the analogue experiment.

Experiment	(°)	Extension (mm)	Upper tip (mm)	Surface def.(mm)	E/D ratio*
a)	60	11.5	- 10	-9.3	1.24
b)	""	11.5	- 30	-8.4	1.37
c)	""	11.5	- 45	-7.7	1.49
d)	""	5.0	- 45	-2.3	2.17
e)	""	11.5	- 45	-7.5	1.53
f)	""	8.0	- 45	-4.6	1.74

\* E/D ratio = extension/ surface deformation

Greater burial depth leads to less surface deformation. The width of the fault also seems to affect the surface deformation with a similar pattern, greater width of the fault leads to a greater deformed area. The observed deformation, especially in the early stages, is comparable with observed coseismic deformation. Sub-ellipsoidal deformation is observed, with the depocenter asymmetric towards the upper tip of the fault. The depocenter it's place above the upper tip of the fault. In the realization of our models we have also successfully applied the digital photogrammetry technique. With this technique it was possible to reconstruct the surfaces in very large format with great accuracy. Thanks to the integration with a python code it was possible to automate almost all of the processing procedure, including the removal of the data obtained. Also thanks to the use of Python it was also possible to automate the processing of the data. This methodology could be successfully applied for the realization of other analog models. The methodology perfected



for this chapter shows a versatility and a precision far superior to the structured light previously used in the analogue modeling laboratory of the Department of Earth and Environmental Sciences of the University of Pavia.

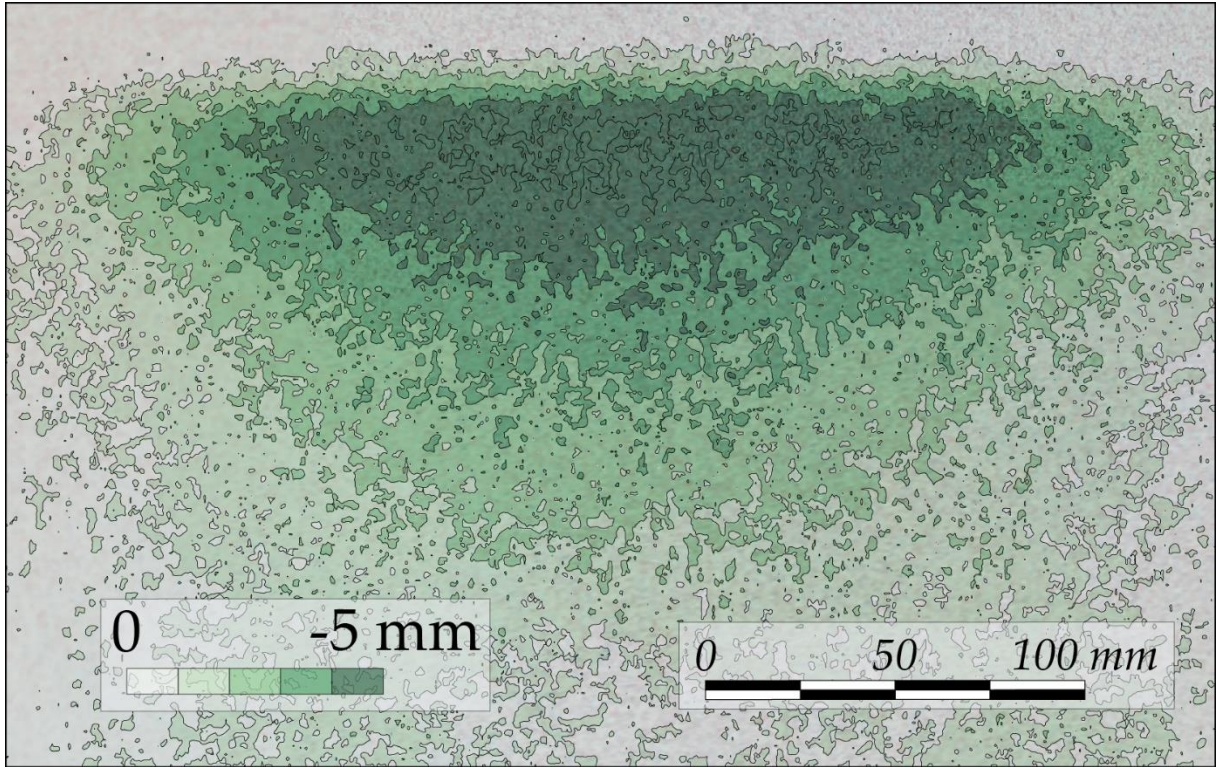


Figure 2.5. Maps showing the initial deformation of experiment c . Extension is toward south.

## References

1. BARNHOORN, A. BYSTRICKY, M., BURLINI, L. & KUNZE, K. 2004. The role of recrystallization on the deformation behaviour of calcite rocks: large strain torsion experiments on Carrara marble. *Journal of Structural Geology*, 26, 885–903.
2. Bemis, S.P., Micklethwaite, S., Turner, D., James, M.R., Akciz, S., Thiele, S.T., & Bangash, H.A. (2014). Ground-based and UAV-based photogrammetry: A multi-scale, high-resolution mapping tool for structural geology and paleoseismology. *Journal of Structural Geology*, 69, 163-178, doi: 10.1016/j.jsg.2014.10.007
3. Biasi, G.P.; Weldon, R.J. Estimating surface rupture length and magnitude of paleoearthquakes from point measurements of rupture displacement. *Bull. Seismol. Soc. Am.* 2006, 96, 1612–1623.
4. Birch, J.S. (2006). Using 3DM Analyst mine mapping suite for rock face characterization, In F. Tonon and J. Kottenstette (eds.), *Laser and Photogrammetric Methods for Rock Face Characterization*, Proc. 41st U.S. Rock Mechanics Symp., Golden.
5. Bonanno, E.; Bonini, L.; Basili, R.; Toscani, G.; Seno, S. How do horizontal, frictional discontinuities affect reverse fault-propagation folding? *J. Struct. Geol.* 2017, 102, 147–167.
6. Bonini, L.; Basili, R.; Toscani, G.; Burrato, P.; Seno, S.; Valensise, G. The role of pre-existing discontinuities in the development of extensional faults: An analog modeling perspective. *J. Struct. Geol.* 2015, 74, 145–158.
7. Bonini, L.; Basili, R.; Toscani, G.; Burrato, P.; Seno, S.; Valensise, G. The effects of pre-existing discontinuities on the surface expression of normal faults: Insights from wet-clay analog modeling. *Tectonophysics* 2016, 684, 157–175.
8. BYERLEE, J. 1978. Friction of rocks. *Pure and Applied Geophysics*, 116, 615–626.
9. Bürgmann, R.; Pollard, D.D.; Martel, S.J. Slip distributions on faults: effects of stress gradients, inelastic deformation, heterogeneous host-rock stiffness, and fault interaction. *J. Struct. Geol.* 1994, 16, 1675–1690.
10. Cadell, H.M. VII.—Experimental Researches in Mountain Building. *Trans. R. Soc. Edinburgh* 1889, 35, 337–357.
11. CASAGRANDE, A. 1932. Research on the Atterberg limits of soils. *Public Roads*, 13(9), 121–136.



12. Cavinato, G.P.; De Celles, P.G. Extensional basins in the tectonically bimodal central Apennines fold-thrust belt, Italy: Response to corner flow above a subducting slab in retrograde motion. *Geology* 1999, *27*, 955–958.
13. Cavinato, G.P.; Carusi, C.; Dall’asta, M.; Miccadei, E.; Piacentini, T. Sedimentary and tectonic evolution of Plio-Pleistocene alluvial and lacustrine deposits of Fucino Basin (central Italy). *Sediment. Geol.* 2002, *148*, 29–59.
14. Cooke, M.L.; Schottenfeld, M.T.; Buchanan, S.W. Evolution of fault efficiency at restraining bends within wet kaolin analog experiments. *J. Struct. Geol.* 2013, *51*, 180–192.
15. Cooke, M.L.; Van Der Elst, N.J. Rheologic testing of wet kaolin reveals frictional and bi-viscous behavior typical of crustal materials. *Geophys. Res. Lett.* 2012, *39*. Francioni et al., 2017
16. Graveleau, F.; Malavieille, J.; Dominguez, S. Experimental modelling of orogenic wedges: A review. *Tectonophysics* 2012, *538–540*, 1–66.
17. Improta, L.; Villani, F.; Bruno, P.P.; Castiello, A.; De Rosa, D.; Varriale, F.; Punzo, M.; Brunori, C.A.; Civico, R.; Pierdominici, S.; et al. High-resolution controlled-source seismic tomography across the Middle Aterno basin in the epicentral area of the 2009, Mw 6.3, L’Aquila earthquake (central Apennines, Italy). *Ital. J. Geosci.* 2012, *131*, 373–388.
18. Jackson, J.A.; White, N.J. Normal faulting in the upper continental crust: observations from regions of active extension. *J. Struct. Geol.* 1989, *11*, 15–36.
19. King Hubbert, M. Theory of scale models as applied to the study of geologic structures. *Bull. Geol. Soc. Am.* 1937, *48*, 1459–1520.
20. Kim, Y.S.; Sanderson, D.J. The relationship between displacement and length of faults: A review. *Earth-Science Rev.* 2005, *68*, 317–334.
21. Koyi, H. Analogue modelling: From a qualitative to a quantitative technique - A historical outline. *J. Pet. Geol.* 1997, *20*, 223–238.
22. Lohrmann, J.; Kukowski, N.; Adam, J.; Oncken, O. The impact of analogue material properties on the geometry, kinematics, and dynamics of convergent sand wedges. *J. Struct. Geol.* 2003, *25*, 1691–1711.
23. Lowe, D.G. (1999). Object recognition from local scale-invariant features. In *Computer vision, 1999. The proceedings of the seventh IEEE international conference on* (Vol. 2, pp. 1150-1157). IEEE.

24. Lowe, D.G. (2004). Distinctive image features from scale-invariant keypoints. *International journal of computer vision*, 60(2), 91-110.
25. McClay, K.R. Extensional fault systems in sedimentary basins: a review of analogue model studies. *Mar. Pet. Geol.* 1990, 7, 206–233.
26. MARONE, C. 1998. Laboratory-derived friction laws and their application to seismic faulting. *Annual Review of Earth and Planetary Sciences*, 26, 643–696.
27. Menegoni, N.; Meisina, C.; Perotti, C.; Crozi, M. Analysis by UAV digital photogrammetry of folds and related fractures in the monte antola flysch formation (Ponte organasco, Italy). *Geosci.* 2018,
28. Menegoni, N.; Giordan, D.; Perotti, C.; Tannant, D.D. Detection and geometric characterization of rock mass discontinuities using a 3D high-resolution digital outcrop model generated from RPAS imagery – Ormea rock slope, Italy. *Eng. Geol.* 2019, 252, 145–163.
- Spetsakis, M., & Aloimonos, J.Y. (1991). A multi-frame approach to visual motion perception. *International Journal of Computer Vision*, 6(3), 245-255.
29. PANIEN, M. 2004. Analogue modelling experiments of basin inversion using well-characterized granular materials and comparisons with numerical models. Ph.D. thesis. University of Bern, Switzerland.
30. Panara; Toscani; Cooke; Seno; Perotti Coseismic Ground Deformation Reproduced through Numerical Modeling: A Parameter Sensitivity Analysis. *Geosciences* 2019, 9, 370.
31. Ramberg, H. Gravity, deformation and the earth's crust. In theory, experiments and geological application, second edition. *Gravity, Deform. earth's crust. theory, Exp. Geol. Appl. Second Ed.* 1981.
32. Rupnik, E., Daakir, M., & Deseilligny, M.P. (2017). MicMac—a free, open-source solution for photogrammetry. *Open Geospatial Data, Software and Standards*, 2(1), 14.
33. Schellart, W.P. Shear test results for cohesion and friction coefficients for different granular materials: Scaling implications for their usage in analogue modelling. *Tectonophysics* 2000, 324, 1–16.
34. Schreurs, G.; Buitter, S.J.H.; Boutelier, D.; Corti, G.; Costa, E.; Cruden, A.R.; Daniel, J.M.; Hoth, S.; Koyi, H.A.; Kukowski, N.; et al. Analogue benchmarks of shortening and extension experiments. *Geol. Soc. Spec. Publ.* 2006, 253, 1–27.
35. Schulze, D. Entwicklung und Anwendung eines neuartigen Ringschergeraetes. *Aufbereitungs-Technik* 1994, 35, 524.

36. Stewart, J.H. Basin and range structure: A system of horsts and grabens produced by deep-seated extension. *Bull. Geol. Soc. Am.* 1971, 82, 1019–1044.
37. Stewart, J.H. Basin-range structure in western North America: A review. In Proceedings of the Memoir of the Geological Society of America; 1978; Vol. 152, pp. 1–31.
38. Sturzenegger, M., Stead, D. (2009). Close-range terrestrial digital photogrammetry and terrestrial laser scanning for discontinuity characterization on rock cuts. *Engineering Geology*, 106, 163–182, doi:10.1016/j.enggeo.2009.03.004
39. Thielicke, W., 2014. The Flapping Flight of Birds – Analysis and Application, Phd thesis, Rijksuniversiteit, Groningen.
40. Thielicke, W., Stamhuis, E.J., 2014. PIVlab – Towards User-friendly, Affordable and Accurate Digital Particle Image Velocimetry in MATLAB. *Journal of Open Research Software*, 2(1):e30, doi: <http://dx.doi.org/10.5334/jors.bl>.
41. Turner et al., 2014]
42. Van Rossum, 1991
43. Wu, C., Agarwal, S., Curless, B., & Seitz, S.M. (2011, June). Multicore bundle adjustment. In *Computer Vision and Pattern Recognition (CVPR), 2011 IEEE Conference on* (pp. 3057-3064). IEEE.
44. Wu, C. (2013, June). Towards linear-time incremental structure from motion. In *3D Vision-3DV 2013, 2013 International Conference on* (pp. 127-134). IEEE.
45. Gorceix, C., 1924. Expériences de laboratoire sur la formation des montagnes. *Revue de Géographie Alpine* 12 (1), 31–78.
46. Paulcke, W., 1912. Das Experiment in der Geologie. Festschrift zur Feier des fünfündfünfzigsten Geburtstages Seiner Königlichen Hohiet des Großherzogs Friedrich II, Karlsruhe, pp. 74–108.
47. Summers, H.S., 1933. Experimental Tectonic Geology. Meeting of the Australian and New Zealand Association for the Advancement of Science, pp. 49–75.
48. Wells, D.L.; Coppersmith, K.J. New empirical relationships among magnitude, rupture length, rupture width, rupture area, and surface displacement. *Bull. - Seismol. Soc. Am.* 1994, 84, 974–1002.

---

## Chapter 3. Numerical models

# Coseismic Ground Deformation Reproduced through Numerical Modeling: A Parameter Sensitivity Analysis

Yuri Panara <sup>1,\*</sup>, Giovanni Toscani <sup>1,3</sup>, Michele L. Cooke <sup>2</sup>, Silvio Seno <sup>1,3</sup> and Cesare Perotti <sup>1,3</sup>

Department of Earth and Environmental Sciences, University of Pavia, Pavia I-27100, Italy

Department of Geosciences, University of Massachusetts, Amherst, MA 01003, USA

CRUST (Centro interUniversitario per l'analisi SismoTettonica tridimensionale con applicazioni territoriali), Pavia I-27100, Italy

*Geosciences* 2019, 9, 370; doi:10.3390/geosciences9090370

**Abstract:** Coseismic ground displacements detected through remote sensing surveys are often used to invert the coseismic slip distribution on geologically reliable fault planes. We analyze a well-known case study (2009 L'Aquila earthquake) to investigate how three-dimensional (3D) slip configuration affects coseismic ground surface deformation. Different coseismic slip surface configurations reconstructed using aftershocks distribution and coseismic cracks, were tested using 3D boundary element method numerical models. The models include two with slip patches that reach the surface and three models of blind normal-slip surfaces with different configurations of slip along shallowly-dipping secondary faults. We test the sensitivity of surface deformation to variations in stress drop and rock stiffness. We compare numerical models' results with line of sight (LOS) surface deformation detected from differential SAR (*Synthetic Aperture Radar*) interferometry (DInSAR). The variations in fault configuration, rock stiffness and stress drop associated with the earthquake considerably impact the pattern of surface subsidence. In particular, the models with a coseismic slip patch that does not reach the surface have a better match to the line of sight coseismic surface deformation, as well as better match to the aftershock pattern, than models with rupture that reaches the surface.

The coseismic slip along shallowly dipping secondary faults seems to provide a minor contribution toward surface deformation.

Keywords: coseismic ground deformation; active fault geometry; DInSAR; numerical models; sensitivity analysis

### 3.1. Introduction

Understanding the relationships between subsurface slip and coseismic ground deformation provides a foundation for many seismotectonic and seismic hazard assessment studies. Starting from the work of Massonnet in 1993 [1], remote sensing techniques have provided new important tools for the detection, observation and measurement of surface coseismic deformation (e.g., [2–5]). Differential SAR (*Synthetic Aperture Radar*) interferometry (DInSAR) analysis can measure coseismic surface deformation (e.g., [6]) and consequently, serve as input data for numerical models that invert for fault geometry and/or fault slip distribution (e.g., [2,3,5,7]). If fault geometry is well constrained, the inversions can produce reliable slip distributions that are consistent with seismic data [2,7]; for this reason, we used geologic and geophysical data in order to constrain a reliable fault configuration.

The L'Aquila seismic sequence (Figure 3.1) occurred in a seismically active region of central Italy on April 6, 2009 (Table 3.1). Despite the large amount of data collected (aftershock distribution, coseismic cracks and focal mechanism) and interpretations made, several uncertainties persist about the deep geometry of the fault responsible for the L'Aquila earthquake and on the interpretation of rupture surface geometry associated with the earthquake.

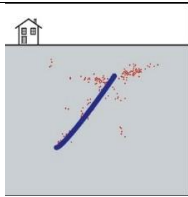
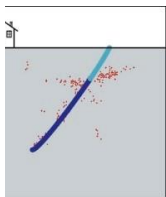
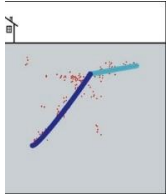
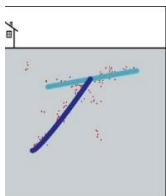
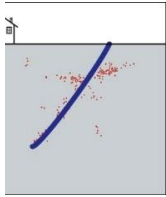
Table 3.1. Main historical seismic events in the L'Aquila area [8].

MwM	Epicentral Area	Year
6.10	L'Aquila region	2009
5.02	L'Aquila region	1958
5.27	Mt. Gran Sasso	1951
5.7	Mt. Gran Sasso	1950
5.05	L'Aquila region	1916
5.33	L'Aquila	1791
6.67	L'Aquila region	1703
5.33	Monti della Laga	1672
5.33	L'Aquila region	1619
6.5	L'Aquila region	1461
5.56	L'Aquila region	1315

The aftershocks [9], focal mechanism [10], surface deformation detected from DInSAR [2,5,7], GPS measurement inversion [11], and coseismic surface cracks [12] do not converge on a single subsurface slip patch geometry for the L'Aquila earthquake [11,13–17]. Some studies suggest that the coseismic slip along the Paganica fault reached the Earth's surface [14,18], while other studies infer that the rupture was blind [16]. Furthermore, aftershocks suggest the potential involvement of shallow-dipping thrust faults that may have been reactivated with normal slip [15,16].

In this research, using aftershocks' locations associated with the L'Aquila 2009 earthquake [19,20] and coseismic cracks [12], we reconstructed five different slip surface configurations possibly associated with the seismic sequence (Table 3.2). The five plausible geometries are based on previous interpretations [13–16]; however, we reconstructed the three-dimensional fault geometries directly from both geologic and geophysical data.

Table 3.2. Two-dimensional (2D) vertical cross sections of five different fault configurations considered for the models. The dark blue normal faults have applied dip-slip shear stress drop of 1.5–4.5 MPa within the numerical models, the light blue faults freely slip in response to the main fault slip.

Cases	2D Section	Description
Case 1		Only the main blind normal fault.
Case 2		The main normal fault was extended to reach the surface coseismic ruptures [12]. This extension is independent from the main fault and represents a passive propagation towards the ground surface.
Case 3		The main normal fault is intersected at its upper tip by a low angle fault. This low angle fault is considered a thrust passively reactivated in extension only in the hanging wall of the main fault.
Case 4		The main normal fault interacts with and passively reactivates a low angle fault. For case 4 we propose a complete thrust passive extensional reactivation near the main faults.
Case 5		The main normal fault reaches the surface in correspondence of the coseismic ground ruptures.

We simulate coseismic deformation along these faults using forward three-dimensional boundary element method (BEM) models. One advantage of this approach over previously performed inversions is that the three-dimensional models incorporate non-planar fault configurations. We assess the sensitivity of slip patch geometry on the pattern of surface displacement, but due to the non-uniqueness of this assessment, we also consider the effect of host rock stiffness (Young' s modulus) and coseismic stress drop on

the ground deformation. We expect that increasing the applied stress drop increases the coseismic slip on the faults and the amplitude of surface displacement. In contrast, increasing host rock stiffness decreases fault slip and surface displacement. Consequently, we expect the models to have a trade-off in match to observation with lesser or greater stress drop and host rock stiffness. For this reason, we assess all five models through a range of reasonable stress drop and host rock stiffness parameter space. In order to constrain the subsurface coseismic slip surface configuration, we compare the surface displacements of the suites of models with line of sight measurements observed from DInSAR satellite [2]. The results of this sensitivity analysis show that the best fit between model results and observed surface deformation occurs for models where slip patch does not reach the surface; for these cases the numerical model results are consistent with the DInSAR displacements.

### 3.1.1. Study Area

The Apennines have a complex structure resulting from a long and composite geological history with the overprinting of different tectonic phases through time. The L'Aquila region was part of the African passive margin of the Ligurian-Piedmont Ocean in the Early Mesozoic, hosting wide carbonate platforms and pelagic basins that underwent the Triassic–Jurassic rifting [21,22]. The successive convergence between African and Eurasian plates began during the Cretaceous, leading to the formation of thrust systems and related foredeep basins that developed up to the Middle Pleistocene migrating towards the Adriatic Sea [23–26]. The core of central Apennines has been affected in the last ~2.5 Ma by SW-NE oriented extension, leading to normal faulting, that today characterizes the whole region [27–29]. Late Quaternary extensional faulting drives the development of shallow intermountain basins with a sediment thickness underneath L'Aquila of up to ~250 m (Figure 3.1) [30].

The current rate of overall extension in the central part of the Apennine, is 2–3 mm/year [31]. The L'Aquila earthquake occurred along the Paganica–S. Demetrio fault, which is one of the NW-SE striking normal faults that accommodates the Apennine



extension [32,33]. One result of this overprinted tectonic history is that the older compressional structures can interact and possibly influence the surface deformation due to the currently active extensional faults in the central Apennines region [15,34].

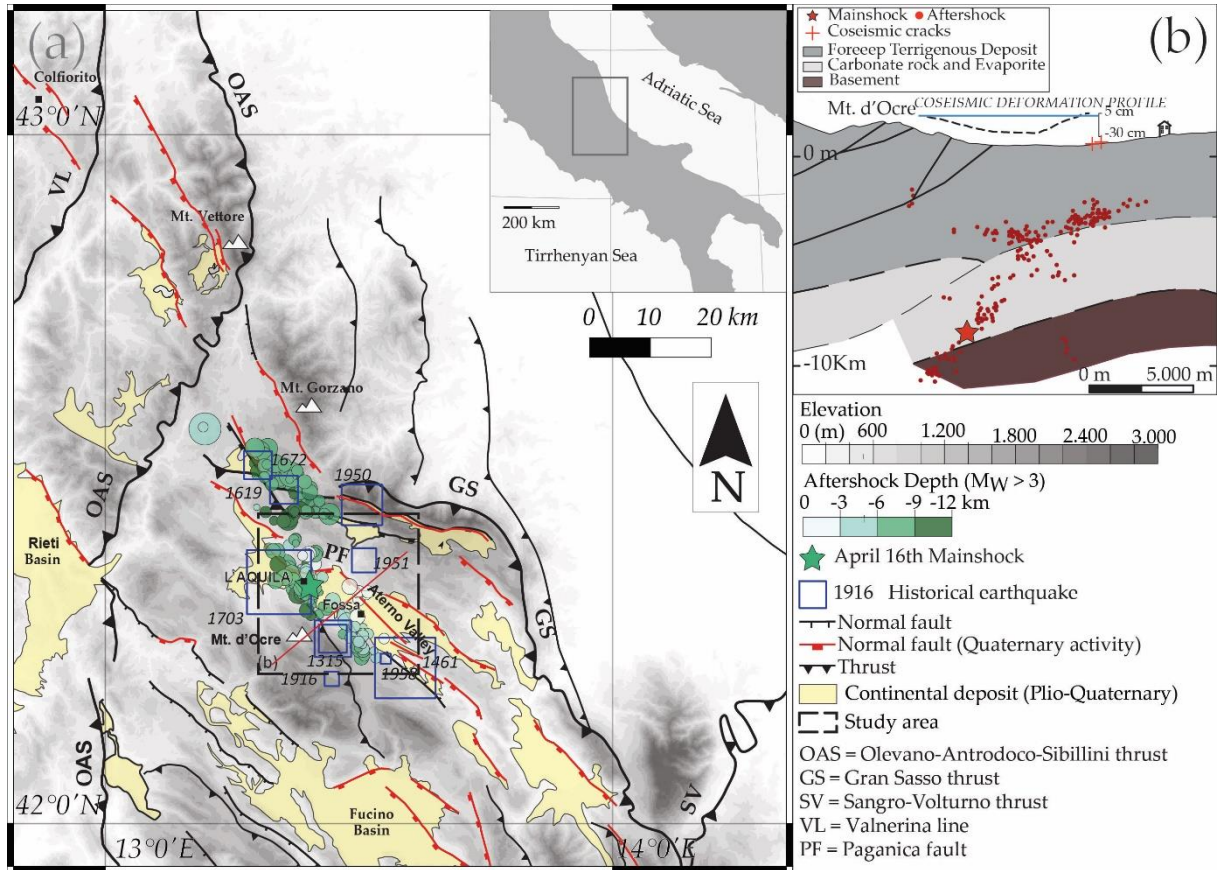


Figure 3.1. (a) Tectonic map of the central Apennines modified after [22] showing the positions of Quaternary intramountain basin and the main aftershocks. The axial part of the Apennines is dominated by thrusting and folding active between Upper Miocene and Middle Pleistocene, successively intersected by normal faults. (b) SW-NE geological section of the L'Aquila area modified after [16]. Relocated aftershocks [9], mapped coseismic cracks [12].

### 3.1.2. L'Aquila Seismic Sequence

On April 6, 2009 a Mw 6.3 earthquake struck the L'Aquila region as part of a long foreshock-aftershock sequence [9,19,20]. A dense local network composed of 67 three-component seismic stations detected the events; twenty of these stations are permanent stations of the Italian Seismic National Network (RSNC) and forty-seven were temporary stations installed after the mainshock to record the aftershock sequence [35]. Significant historical earthquakes in the region (Table 3.1 and Figure 3.1) occurred in 1461 ( $M = 6.4$ ), 1703 ( $M = 6.7$ ), and more recently in 1916 and 1958 [8,36]. Different interpretations were proposed for the geometry of the fault responsible of the 2009 event; most authors proposed a normal fault striking  $130^{\circ}$ – $135^{\circ}$  N and dipping  $45^{\circ}$ – $55^{\circ}$  toward SW with the lower tip at about 11–12 km below the surface (see [13] for a review). These reconstructions were carried out with various techniques using relocated aftershocks [19,20], GPS data inversion [11,37–39] or GPS and DInSAR inversion combined [2,5,7]. Field observations detected a localized network of small surface cracks (open fractures or minor dislocations) mainly along pre-existing faults [40]. The coseismic cracks were observed on three different non-continuous alignments with several gaps between sections of the crack zone, and the total zones' length was 13 km [12]. The most evident zone totaled 5–7 km in length along the northern part of the Paganica–S. Demetrio fault system [12]. Focal mechanisms confirm movement along a normal fault in agreement with the current extension tectonic regime of the area [10]. Most of the focal mechanism solutions of the aftershocks show a normal faulting in agreement with the tectonic setting of the area [10] and describe a fault with dip of about  $50^{\circ}$  and a strike of about  $N135^{\circ}$  E [10].

## 3.2. Surface and Subsurface Data

To reconstruct the geometry of the faults responsible for the 2009 event in L'Aquila area, we combined available seismological and geological data: the aftershocks hypocentral distribution [9] and the surface coseismic cracks (Figure 3.2) [12]. We used the coseismic ground deformations detected from DInSAR as independent data to assess the predictions

of the numerical models. Combining SAR deformation with the observed coseismic cracks is an approach successfully used in previous published work [41].

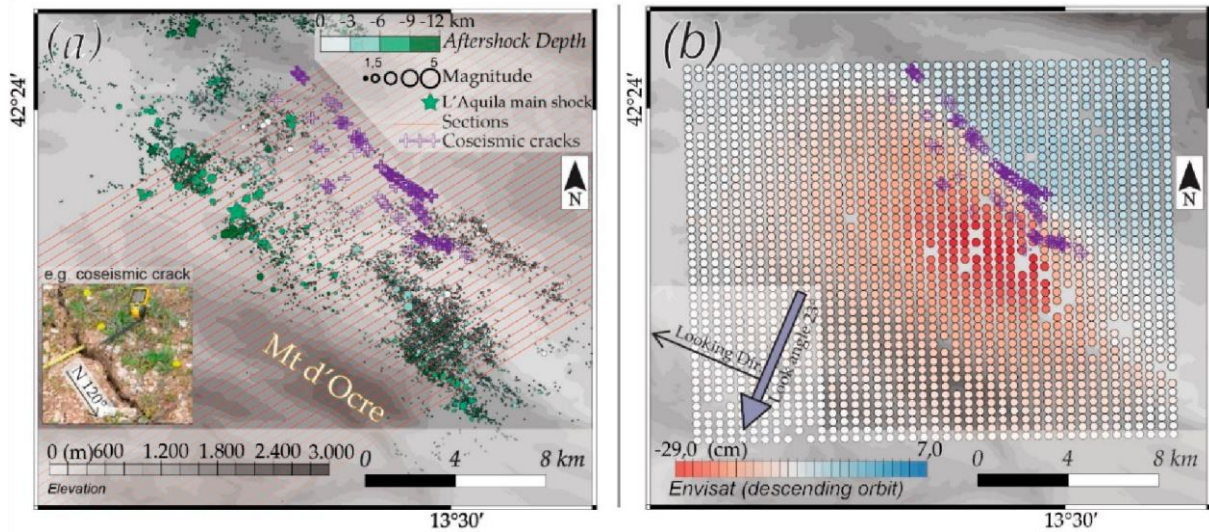


Figure 3.2. Digital elevation model of the study area with the projection of: (a) location and depth of the  $M > 1.5$  aftershocks [9] and the coseismic cracks [12]; (b) coseismic surface line of sight displacements observed from Envisat (descending orbit).

### 3.2.1. Surface Data

Coseismic surface cracks affected an area of more than 100 km<sup>2</sup> around L'Aquila [12,40]. A set of 237 surface cracks were mapped within a 13-km-long zone that strikes between 130 and 140° N [12] and bounds a tectonic basin filled with Quaternary deposits [34,42]. Different types of ground deformations were mapped: coseismic fractures and surface deformation. Along the coseismic fractures, the observed slip varies between zero up to a few centimeters along fractures that dip between 60° and 80°, while measured openings vary between ~1 and 2.5 cm [12,43]. Coseismic cracks (Figure 3.2) were mapped along contacts between different near-surface lithologies. The differences in material properties, between poorly consolidated and unconsolidated alluvium, could possibly play a role in the development of the observed cracks [12].

DInSAR (differential SAR interferometry) techniques record the ground coseismic deformation in the direction of the satellite look angle (e.g., [1]). Here, we used the Envisat data (descending orbit) published by Atzori et al. [2] to constrain between alternative

subsurface coseismic slip patch configurations. Using the April 27, 2008–April 12, 2009 pair acquired descending Envisat orbit (right look angle of 23° and 41 m perpendicular baseline) integrated with GPS data [2], we determined the coseismic ground deformation associated with the L'Aquila earthquake. This interferogram does not show deformation except for the L'Aquila event and is consistent with the interferograms (Envisat ascending and CosmoSkymed ascending) published by Atzori [2]. The maximum observed line of sight displacement occurred between the cities of L'Aquila and Fossa with movement away from the satellite of up to 29 cm [2]. The DInSAR analysis did not show a sharp change in displacement that would indicate a shallow slip [2]. If the fault rupture breaks the ground surface we would expect maximum surface displacement along the fault, which would produce maximum and minimum line of sight displacements very near to the fault trace. Instead, the minimum and maximum are separated by 5–6 km. For this reason, several of the best-fitting inversions to the DInSAR data have little slip along the Paganica fault near the Earth's surface [5]. The area of maximum deformation measured by the interferogram (Figure 3.2) does not correlate with the position of the coseismic cracks [44]. Furthermore, small-wavelength displacement anomalies associated with coseismic cracks show local lowering up to a few centimeters [44], however this local subsidence does not influence the longer wavelength displacement across the area [44]. This local subsidence near surface cracks is an order of magnitude lower than the larger-scale subsidence in the hanging wall of the fault and is also very localized [12].

### 3.2.2. Aftershock Data

A catalogue of more than 50,000 relocated aftershocks [9], spanning from April to December 2009, was used to reconstruct plausible fault configurations (Figure 3.3).

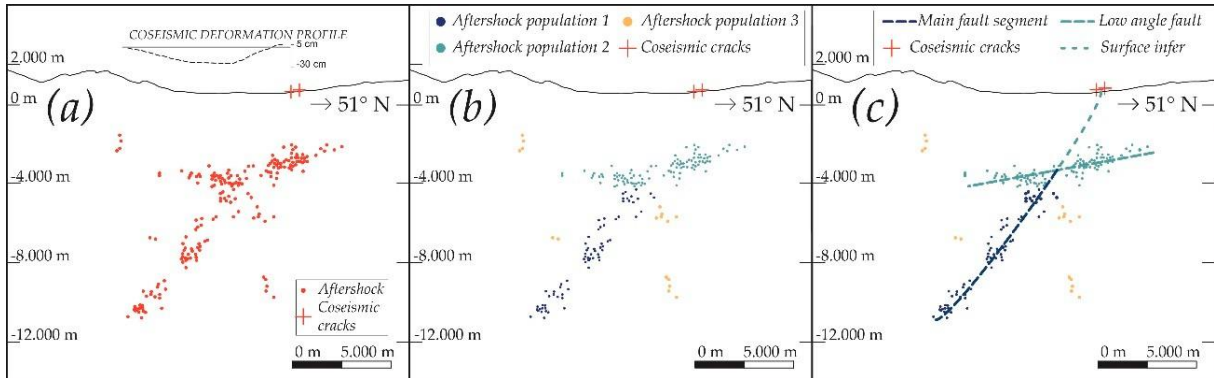


Figure 3.3. Cross section showing (a) aftershocks distribution [9] and coseismic cracks [12]; (b) different populations of aftershocks are shown in dark and light blue; (c) possible coseismic fault geometries interpreted to fit the data. The interpretation of the L'Aquila main fault segment was based on aftershock population 1 (dark blue); population 2 (light blue) was associated with a shallow low angle secondary fault and population 3 was associated with minor structures. The surface projection connects the main fault upper tip to the coseismic surface cracks.

Aftershocks, between 4 and 11 km in depth, appear aligned along a sub-planar surface dipping  $50^{\circ}$ – $55^{\circ}$  to the SW and extending 17–18 km in a NW-SE direction. The rock volume affected by the aftershocks varies in width along strike from 0.3 to 1.5 km [9]. The estimated median error for aftershock distribution is 0.024 km on X easting axis, 0.015 km on Y northing axis, and 0.027 on Z vertical axis km, while the mean errors are 0.178, 0.039, and 0.087 km, respectively [9]. The aftershocks primarily occur between 4 and 10 km in depth; only very few events occur between the surface and 2 km in depth or below 12 km [9,19,20,45]. Over 80% of aftershocks, including major events, are deeper than 4 km [44], which suggests that rupture may not have extended to shallow depth. Between 3 and 12 km of depth many aftershocks align along a sub-planar surface dipping  $50^{\circ}$ – $55^{\circ}$  to the SW and striking NW-SE. We recognized this cluster (population 1) throughout the study area. Between 2 and 4 km depth, a second population of aftershocks (population 2) are aligned



along a sub-planar surface dipping  $\sim 10^\circ$  to the SW and extending in the NW-SE direction. Population 2 is composed of less events than population 1, despite being clearly recognized all along the study area. Lastly, some aftershocks are grouped in small clusters lacking lateral continuity (population 3). These small clusters do not occur in continuity with the main fault and were too small to be connected to significant tectonic structures. For these reasons, population 3 will not be considered in our interpretation (Figure 3.3). The large number of aftershocks within the days following the mainshock do not show a migration of the aftershock spatial distribution. Aftershocks are evenly distributed between high-angle and low-angle fault lines over the time of the observation. For this reason, we use all of the aftershock dataset, in order to better constrain the faults geometries (Figure 3.4).

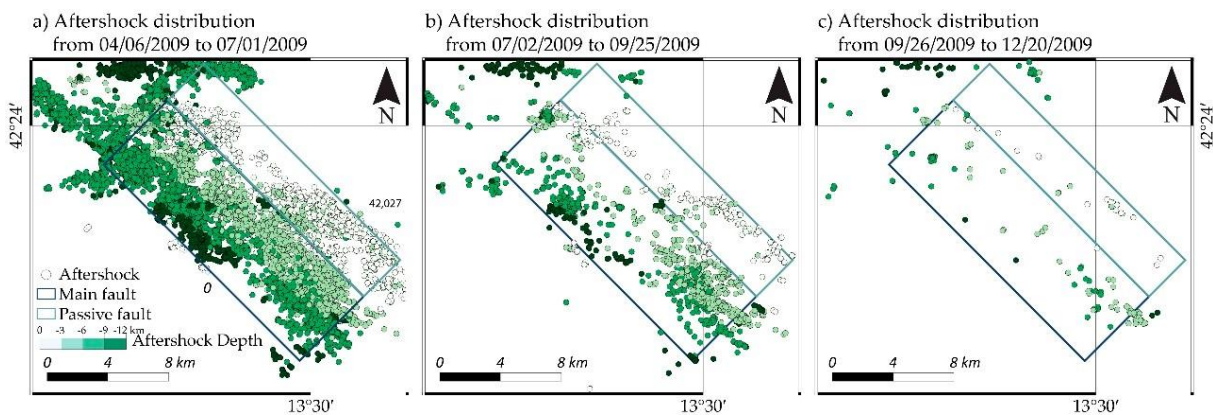


Figure 3.4. Maps view of the aftershock distribution from 04/06/2009 to 12/20/2009. While the number of aftershocks decreases over time, there is no significant evolution of the spatial distribution of the shocks.

### 3.3. Methodology

#### 3.3.1. Fault Construction

We have collected and geo-referenced the available aftershock data using Move™ software (Petroleum Experts). Observing aftershock distribution, we have reconstructed two fault surfaces: the main surface from aftershock population 1 and a secondary fault from population 2 that at shallower depths, has similar strike but a lower dip. We projected aftershocks and ground cracks into forty cross sections, 500 m laterally spaced and

perpendicular to the orientation of the aftershock distributions, which is about  $130^\circ$  N, a trend very close to the alignment of the coseismic crack zone. The aftershock population 1 (Figure 3.3), which is conspicuous all along the study area, constrained our three-dimensional (3D) reconstruction of the Paganica fault plane responsible for the L'Aquila earthquake [2,46]. On each section, we manually selected the aftershocks belonging to population 1 and, using a linear regression automatic fitting tool, which estimates the fault segment using the average position of each aftershock population, we traced a 2D fault segment representing the best fit of the aftershocks.

Interpolation of all the reconstructed segments led to a three-dimensional fault surface representing the portion of the Paganica fault that slipped during the L'Aquila earthquake. This constructed fault surface is sub-planar and extends from 3 to 11 km in depth with a total along strike length of 18 km, overall strike of  $130^\circ$ – $135^\circ$  and dip of  $50^\circ$ – $55^\circ$  towards the SW. We applied the same approach to construct a three-dimensional secondary fault surface from the aftershock population 2 (Figure 3.3). The fault plane strikes  $130^\circ$ – $135^\circ$ , parallel to the main one and shows a gentle dip ( $10^\circ$ ) towards the SW. We also reconstructed a third fault representing the potential connection of the main fault to the surface. To do this, we connected the upper tip of the main and the coseismic cracks mapped on the ground surface (Figure 3.5).

We use these three fault surfaces to assess the role of the following five different plausible fault configurations on coseismic ground deformation (Figure 3.5):

- Case 1 considers only the main blind normal fault extending from 3 to 11 km of depth;
- Case 2 includes the main fault and its prolongation up to the coseismic cracks mapped by Boncio et al. [12]. This model explores the possibility that coseismic slip along the main fault gives passive deformations along the third fault;
- Case 3 includes the main fault and a portion of the shallower low angle secondary fault. This configuration follows the reconstructions by Bigi et al. [15] and Valoroso et al. [9] that show a pre-existing thrust fault reactivated in extension only in the footwall of the main fault;

- Case 4 considers the main fault and the entire shallower low angle fault. This case follows reconstructions by Bonini et al. [16] that suggest a complete extensional reactivation of the thrust both in the hanging wall and in the footwall of the main fault;
- Case 5 is geometrically coincident with Case 2, but here the plane connected to the surface is not passively activated but it is part of the main fault plane reaching the surface. In this case we follow the conceptual model proposed by [14] where the main normal fault reaches the surface and the coseismic ground cracks are directly connected with the fault responsible for the L'Aquila earthquake.

The faults are not perfectly planar and show along strike variations. These faults are consistent with other reconstructions based on focal mechanism solutions [10], aftershock locations [13,16] and geological observations on the Gorzano fault [5,7,15]. Since no aftershocks were detected in the first km of depth [9,41], we have not considered cases with faults terminated just beneath the surface.



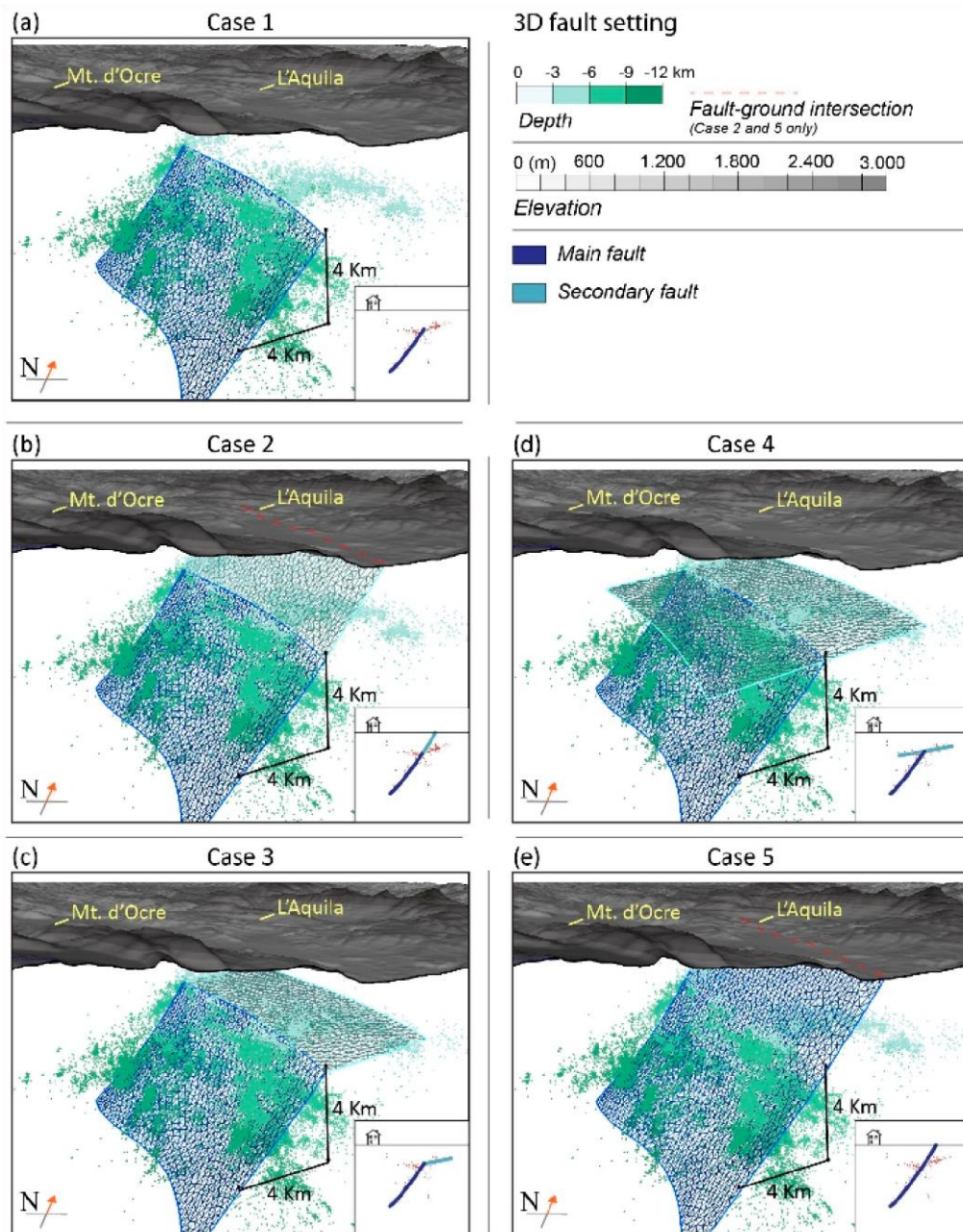


Figure 3.5. 3D view of the five fault configurations of the numerical models with (in green) the aftershock cloud. (a) Case 1: blind active normal fault (dark blue); (b) case 2: blind active normal fault with an passive (light blue) extension to the ground surface (red line); (c) case 3: blind active normal fault with a passive thrust in the footwall; (d) case 4: blind active normal fault with a passive thrust in both foot and hanging wall; (e) case 5: active normal fault reaches the ground surface.

### 3.3.2. Numerical Models

We used numerical models to simulate the surface coseismic deformation of the L'Aquila earthquake associated with the five plausible fault interpretations and compared the resulting ground deformation to line of sight coseismic displacements observed by Envisat satellite. The simulations use Poly3D, a three-dimensional BEM software based on triangular fault elements that allow accurate deformation along non-planar faults [47]. Poly3D has been used to investigate the mechanics of, and interactions among, three-dimensional faults (e.g., [48–53]). Poly3D solves the relevant equations of continuum mechanics to calculate stress and displacements throughout the model [47]. The algebraic expressions for the elastic fields around each element are derived by superposing the solution for an angular dislocation in an elastic half-space [54,55] in the way described by Brown [56] and Jeyakumaran [57]. Stresses and displacements can be reported on both faults and arbitrary observation surfaces. Within Poly3D, faults are discretized within a linear-elastic homogeneous half-space. Poly3D fault models have successfully simulated coseismic surface deformation associated with slip along fault surfaces (e.g., [51,58,59]). For the models of this study, we meshed the fault surfaces (Figure 3.5)

within Poly3D with triangular elements whose sides are 500 m.

For the numerical experiments, we prescribe each fault surface as either active and passive. In the models, active faults that produce L'Aquila mainshock prescribed shear stress drop. Following the approach of Madden and Pollard [51] for simulating coseismic deformation of the Landers 1992 earthquake, we applied a shear traction to the active faults that corresponds to the average shear stress drop of the earthquake. In the models here, in order to simulate the L'Aquila mainshock, we applied dip-slip shear traction to active faults. In contrast, passive faults are those that slip in response to the mainshock [60]. In the numerical models, the passive faults are free to slip (prescribed zero shear traction) in response to the stress drop on the active fault. In cases 1 and 5, a single fault plane is present; for cases 2, 3 and 4, the L'Aquila fault remains active while all the other fault surfaces respond passively (Figure 3.5). In our models, the passive faults are prescribed to be freely-slipping ( $\tau = 0$ ) so

that they slip in response to slip along the normal fault that has applied stress drop. The geological sections available for the area show homogeneous lithologies mostly composed by dolomitic and calcareous deposits, these lithologies have similar stiffnesses with depth [44]. The amount of coseismic surface deformation depends not only on fault geometry but also on values for coseismic stress drop and effective elastic stiffness of the host rock. We test the sensitivity of all five cases to both stress drop and material stiffness. The average stress drop associated with the L'Aquila earthquake was determined using acceleration and velocity waveforms as 2.6 MPa [61], the bulk of the observations varying between 1 and 5 Mpa [61]. To encompass a range of potential values, we varied the stress drop from 1.5 to 4.5 MPa. Trasati et al. [7] used the velocity structure of the region to infer a Lamé lambda constant of 30 GPa and shear modulus of 18 GPa for the upper few km and Lamé constant of 50 GPa and shear modulus of 30 GPa below 10 km depths. From these values, we calculated Young's modulus ranging from 47 to 80 GPa. Other researchers proposed lower stiffness values for sedimentary rocks, between 20 and 45 GPa (e.g., [62]). Due to the wide range in estimated stiffness, we tested a wide range of stiffness values from 20 to 80 GPa and used Poisson's ratio of 0.25 [5,7]. In total, we performed 245 models by testing five different fault configurations, seven stress drop values and seven stiffness values.

### 3.3.3. Line of Sight (LOS) Correction

Each numerical model produces ground deformation associated with the simulated coseismic stress drop. We sampled the model surface deformation at the locations of satellite data information [2]. While the models produced complete three-dimensional displacement fields with east, north and up displacements, the DInSAR data only provided line of sight (LOS) information along the look angle of the satellite. We converted the displacements resulting from the numerical models to the satellite line of sight (LOS) considering both satellite right look angle and satellite 23° direction (Coef. Est, Coef. North and Coef. Up) provided by Atzori [2] and using the formula:

$$LOS = \Delta u_{east} * Coef. East + \Delta u_{north} * Coef. North + \Delta u_{up} * Coef. Up., \quad (1)$$

We assessed the viability of the previously described five cases by comparing the ground deformation patterns from satellite observations and those resulting (and corrected) from model simulations.

### 3.4. Results

To compare the numerical model predictions to the observed ground deformation we subtracted the DInSAR surface displacements from the LOS Poly3D displacements for all the tested fault configurations (Figures 3.6–3.8. See supplementary materials). For each fault configuration (Figure 3.7), we showed the different maps for the range of tested stress drop and stiffness (Figure 3.8) and also showed the median of the net difference maps (absolute value of model – absolute value of observed). For the L’Aquila earthquake, the dominant signal in the ground displacements was away from the satellite movement of the ground surface above the hanging wall of the normal fault (negative displacement Figure 3.6a). The DInSAR also showed a minor deformation towards the satellite ground surface movement of the ground in the footwall of the normal fault.

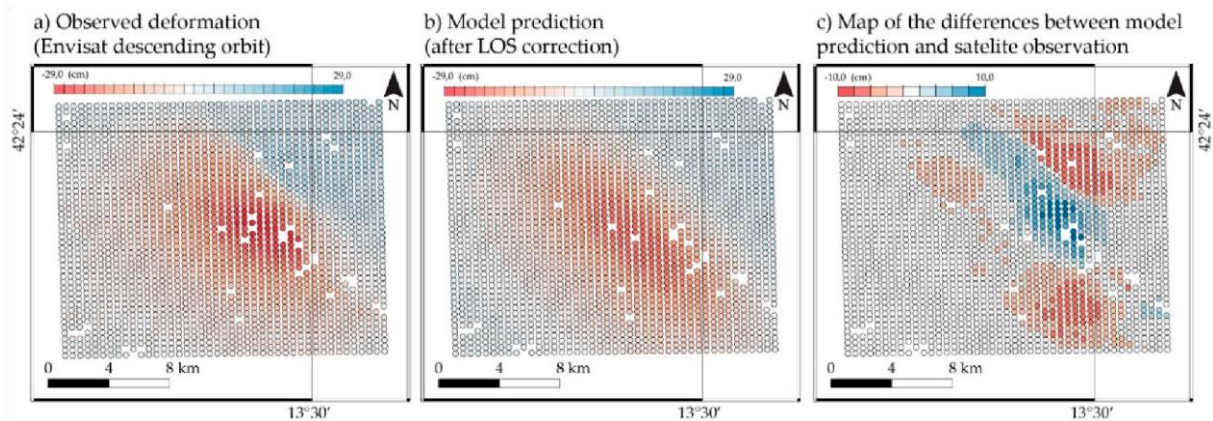


Figure 3.6. Maps showing the conceptual scheme used to calculate the differences between the observed and the modeled surface line of sight (LOS) displacements.

#### 3.4.1. Residual Difference Maps

The comparison between the predicted (model) and observed DInSAR displacements calculated along the line of sight (LOS) of the satellite highlight how fault configurations, stress drop and stiffness affect the surface deformation (Figure 3.7).

Within Figure 7, negative values indicate regions either where the model towards the satellite displacement is less than observed or where model ground displacement away from the satellite is greater than observed.

Case 1 (blind normal fault, Figure 3.7a): Since the away from satellite displacement of the ground above the normal fault's hanging wall dominates the displacement pattern (Figure 3.6a), we will focus the comparison of case 1 surface difference maps to this aspect of the deformation. High stiffness in the models reduce the away from satellite deformation of the ground above the hanging wall of the normal fault. Displacement maps of models with high stiffness in Figure 3.7a have the greatest positive (blue) difference. In contrast, increasing stress drop increases the away from satellite ground displacement above the hanging wall and increasing the stress drop produces more negative difference maps (red). The best match (i.e., models with low differences between model and satellite observations), are those that cross Figure 7a from the upper right to the bottom left where the trade-offs of stiffness and stress drop are balanced. Among these results are models where stress drop values are close to the values inferred for earthquakes similar to the L'Aquila one (2.5–3 MPa) [61,63].



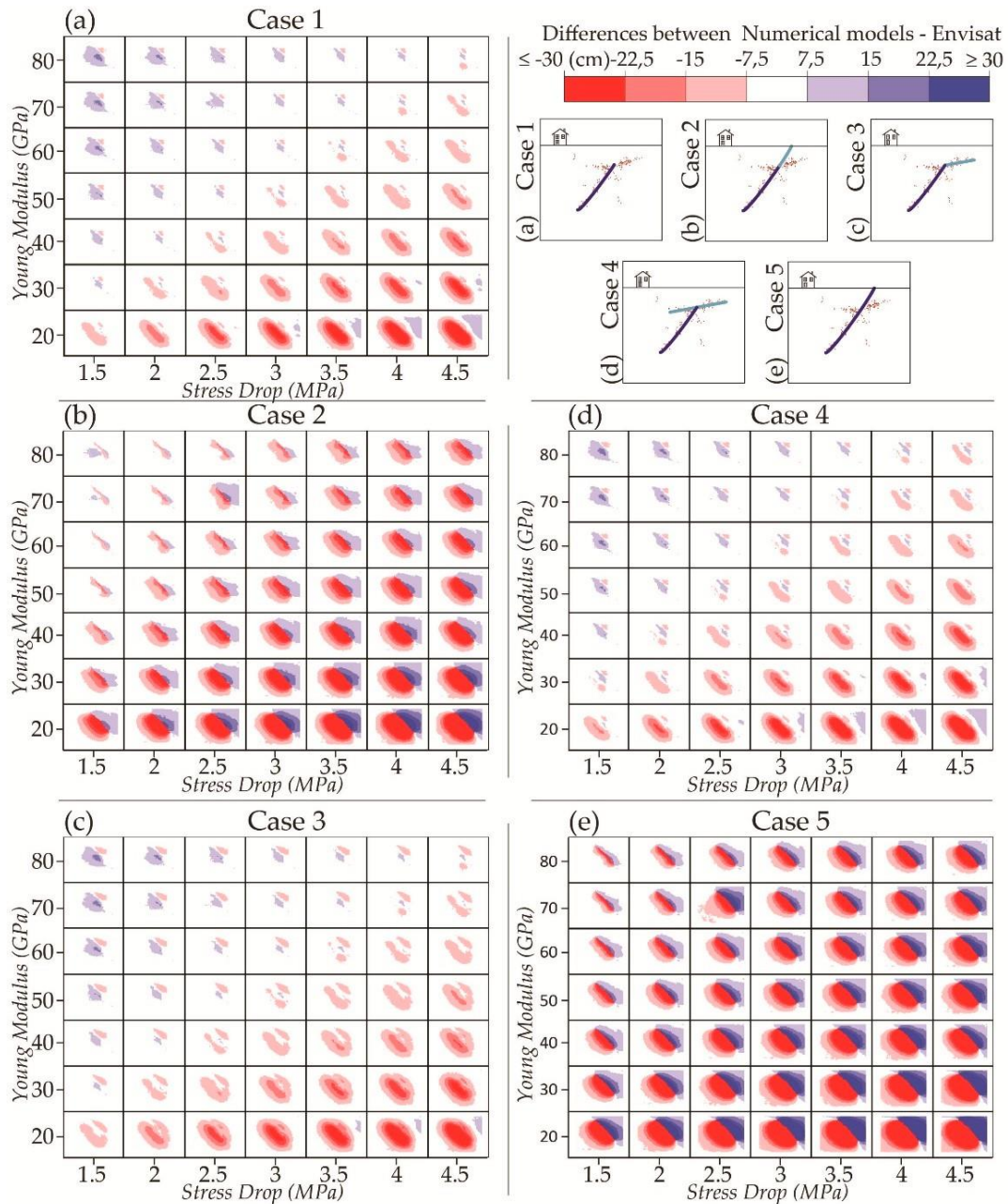


Figure 3.7. Maps of the residual differences between numerical models and satellite observed surface line of sight displacements as calculated in Figure 5. The color scale has been limited to between +20 and -20 cm, and the white area represents a differential deformation <7.5 cm. Subfigures from (a-e) represents a two-dimensional (2D) vertical cross sections of the five different fault configurations.

Case 2 (main fault with passive connection to surface, Figure 3.7b): The model results show the same trends for increasing stress drop and stiffness as case 1, but the balance between the two parameters is reached with minimum mismatch at a relatively low stress drop and

high values of stiffness. According to published data [61], these values may not be representative of this earthquake. Increasing the applied stress drop from 1.5 MPa increases both the away from satellite ground movement in the hanging wall and the towards the satellite movement of the footwall of the normal fault. This outcome is consistent with a greater normal slip on the fault that would increase the downdrop of the footwall and uplift of the hanging wall.

Case 3 (main fault and secondary fault within footwall, Figure 3.7c): The results show a pattern of residual deformation comparable with case 1. A comparison between case 3 and 1 reveals that the presence of the low-angle secondary fault has a small impact on the surface deformation above the footwall region. Slip along the shallower low angle fault in response to stress drop along the main one reduces the towards the satellite ground deformation in the footwall of the main fault. This result is consistent with normal dip-slip along the secondary fault that would pull the overlying rock volume downward relative to case 1 that has no secondary fault.

Case 4 (main fault and complete secondary fault, Figure 3.7d): The results show a differential deformation pattern comparable to case 1 (Figure 7d). At the surface, deformation above the footwall more closely resembles case 1 than case 3, suggesting that the secondary fault slips differently if it extends through both the hanging wall and footwall of the main fault (instead of being limited to the footwall, as in case 3). In case 4, the dip-slip is focused on the portion of the secondary fault in the hanging wall of the main fault. For example, the maximum slip in the model with 3 MPa of stress drop and 50 GPa of stiffness, is 0.35 m in the hanging and 0.16 m in the footwall. Also, the main fault slips more (up to 1.15 m) in case 4 than in either case 1 or 3 (respectively, up to 1.0 and 1.1 m). For models with equal stress drop and stiffness in cases 3 and 4, the model of case 4 produces slightly greater mismatch to satellite observation than case 3.

Case3.5(stress drop applied to a single main fault plane reaching the surface, Figure 3.7e): The resulting difference maps resemble those of case 2 with even greater away from the satellite ground displacement of the footwall. This outcome is consistent with the greater

fault slip as stress drop is applied to a unique outcropping fault plane. The best match of surface displacement within the range of parameters tested is with the lowest stress drop and highest stiffest host rock; however, this difference map does not show as close a match of model and observation as the models with other active fault configurations.

### 3.4.2. Median Net Difference

To assess the overall match of each model with variations of stress drop and stiffness, Figure 8 shows the median difference between the absolute values of the calculated model and the observed displacements.

The use of absolute values of the displacement ensures that areas of positive and negative displacement do not offset one another. While the resulting mismatch values have a very wide range, to better highlight the results with the closest match to satellite observation we limited the color scale to between +20 and -20 cm. The white colors represent net differences lower than 4 cm, indicating the best match between numerical results and observed DInSAR displacements. The purple colors indicate numerical models with median net displacement (both towards and away from the satellite) that exceeds the DInSAR, while the orange colors indicate numerical models with median net displacement that underestimate the DInSAR. Increasing stress drop and decreasing stiffness both increase the ground surface displacements in the numerical models (Figure 3.8). In all diagrams of Figure 3.8 the upper left cases (high stiffness and low stress drop) underestimate the median observed displacements, while the lower right cases (low stiffness and high stress drop) overestimate the surface deformation.

Cases 1, 3 and 4 (blind faults, Figure 3.8a,c,d) show similar distribution of net difference values. The models that show minimum differences are those with a stress drop of 3 MPa and 50 GPa stiffness. In case 5 (outcropping fault) only models with a stress drop of 1.5 MPa and a stiffness of 80 GPa approximate the surface deformations. Case 2 presents results similar to case 5 with the best models' results associated with low stress drop and high stiffness values.



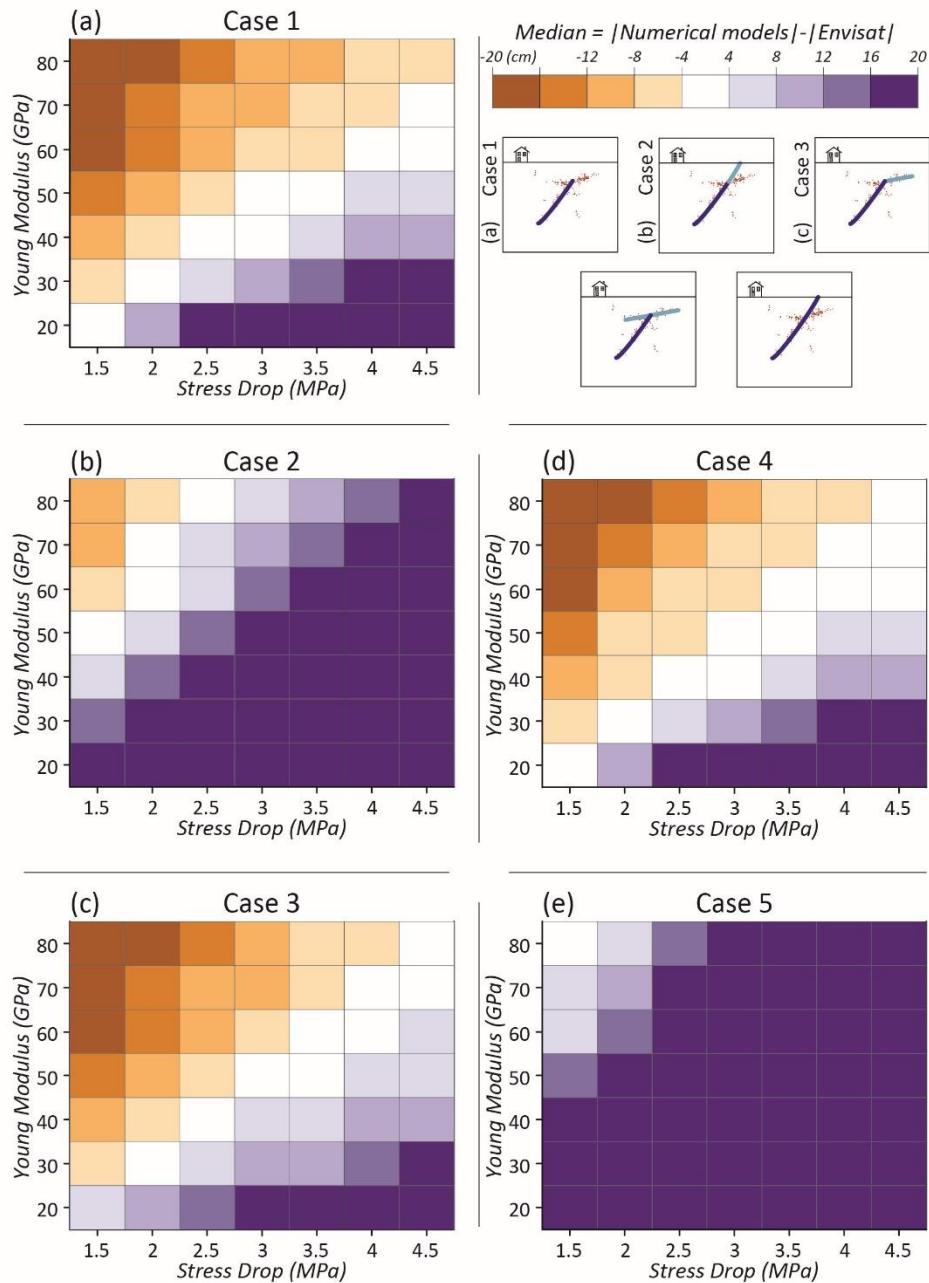


Figure 8. Differences diagram showing the median absolute difference of LOS deformation between numerical models and satellite observation. Subfigures from (a–e) represents a two-dimensional (2D) vertical cross sections of the five different fault configurations.

### 3.5. Discussion

The L'Aquila earthquake, which may have involved slip on several different fault surfaces, may be an example of deformation within early phases young extensional regimes that could involve also pre-existing inherited structures [64]. Despite the wide amount of data collected on the L'Aquila earthquake, multiple subsurface slip surface interpretations

persist. All the reconstructions agree that the L'Aquila seismic sequence was primarily caused by slip along the Paganica normal fault, striking  $130^{\circ}$ – $135^{\circ}$  N with the lower tip of the fault plane at 11–12 km in depth [13]. At shallower depths a wide range of possible slip surface geometries have been proposed [2,14–16]. For example, some proposed slip along a sub-horizontal inherited structure triggered by the interaction with the slip along the main normal fault [15,16], while other studies suggested that the slip propagation on the Paganica fault during the L'Aquila earthquake reached Earth's surface without any interaction with inherited structures [14,18]. The numerical models of this study assess the different slip surface geometries proposed by different authors by comparing the numerical results to independent data on surface ground movement from DInSAR. The numerical results show that, for the range of stress drop and stiffness tested here, models with blind normal faults (cases 1, 3 and 4) better approximate the observed ground deformation [2] than models where faults directly outcrop to the surface (cases 2 and 5; Figure 3.9).

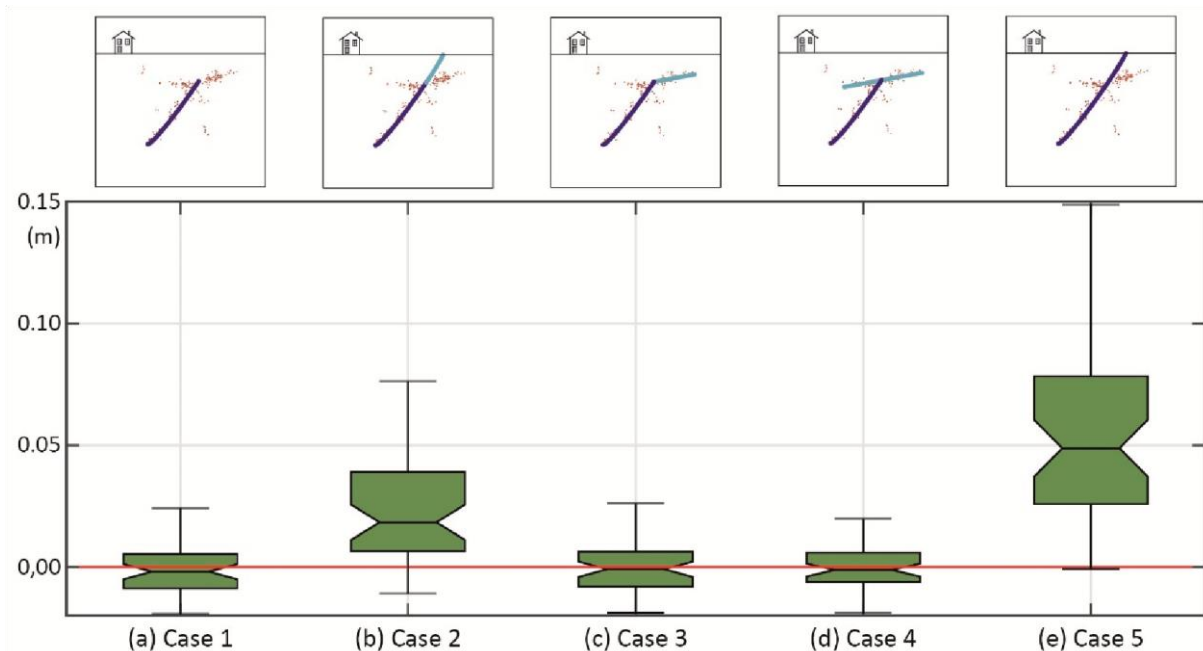


Figure 3.9. Median mismatch, calculated from different maps, for the five considered geological settings. Horizontal black mark indicates the median value; bars are extended on the whole data range from the minimum to the maximum value; the bottom and top edges of

the green area indicate the 25th and 75th percentiles, respectively. The red line indicates zero differences between observed and predicted ground deformation.

The models incorporating an outcropping fault (either passive, case 2, or active, case 5) only reproduce the observed coseismic displacements for a narrow range of stress drop and stiffness that are at or near the bounds of the permissible ranges [7,61,62]. For case 5 (Table 3.3), the only simulation consistent with the observed surface deformation occurs with 80 GPa host rock stiffness and 1.5 MPa stress drop (Figure 3.8), however this stress drop is smaller than that estimated for the L'Aquila earthquake of 2.6 MPa [61]. The models with an outcropping fault seem to not match the surface displacements because the DInSAR data do not show a sharp discontinuity in ground displacements across the projected fault surface traces, and minimum and maximum ground deformation values (-29 and +7 cm) are separated by 5–6 km [2]. The models with a blind fault are consistent with previous inversions from the DInSAR data which show little or no slip from the upper few kilometers [5,7].

Table 3.3. Summary of the characteristics of the best results obtained for the different geometries.

Case	Stress Drop	Rock Stiffness	Maximum Slip	Seismic Moment
Case 1	3.0 MPa	50 GPa	1.0 m	$2.5 \times 10^{18}$ Nm
Case 2	2.5 MPa	80 GPa	0.8 m	$4.0 \times 10^{18}$ Nm
Case 3	3.0 MPa	50 GPa	1.1 m	$3.0 \times 10^{18}$ Nm
Case 4	3.0 MPa	50 GPa	1.2 m	$2.9 \times 10^{18}$ Nm
Case 5	1.5 MPa	80 GPa	0.8 m	$4.4 \times 10^{18}$ Nm

These findings seem to suggest that the fault rupture could have been blind and that both the surface cracks mapped [12] and the observed post-seismic deformation [65] may not reflect coseismic rupture to the Earth's surface. Post-seismic deformation [65] could

include secondary gravitational effects and may not be a direct expression of slip propagation to the ground surface. The good match of numerical models that incorporate blind faults (cases 1, 3 and 4) suggests that an active fault buried 3 km below the surface can replicate ground deformation during the 2009 L'Aquila earthquake. A triggered slip along a synthetic low-angle fault, detected from aftershock distribution, locally impacts the coseismic surface deformation within the footwall [16]; however, this footwall deformation is much smaller than the hanging wall displacements.

We can test if the best fitting models also produce maximum slip and seismic moment that are consistent with observed source parameters and with previous interpretations (Table 3.4). In addition to the average stress drop value for the L'Aquila earthquake of 2.6 MPa [61], the maximum amount of slip on a fault surface is ~1 m [13] and seismic moment is between  $2.9$  and  $3.5 \times 10^{18}$  Nm [2,38]. For cases 1 and 3 (Table 3.3), models with 3 MPa stress drop and 50 GPa Young's modulus, that have a good match to the observed ground displacement, produce maximum slip of ~1 m and seismic moment between  $2.5$  and  $3.0 \times 10^{18}$  Nm corresponding to a 6.3 moment magnitude. The slip amount and observed ground deformation resulting from this model are consistent with observations [2,38]. For case 4, the model with 3 MPa of stress drop and 50 GPa of Young's modulus has good match to the observed ground displacement and the seismic moment is  $2.9 \times 10^{18}$  Nm corresponding to a 6.3 moment magnitude. However, the maximum slip value in this model reaches 1.15 m. It is interesting that this model produces more slip but the same seismic moment. For case 2 (Table 3.3), the model with 2.5 MPa stress drop and 80 GPa stiffness has good correspondence with observed deformation; however, the maximum fault slip is 0.75 m and seismic model is  $4.0 \times 10^{18}$  Nm. While the slip values are lower than those of other models, the seismic moment exceeds both the values from other models and estimates of seismic moment [2,13,38]. Cases 2 and 5 have greater areas of coseismic slip so that even with lesser maximum dip-slip magnitude, the total seismic moment over-predicts the estimates for seismic moment of the L'Aquila earthquake [2,38].

Table 3.4. Summary of the main features of the L'Aquila fault; see [13] for a review.

Author	Maximum Slip	Seismic Moment	Strike	Dip
Atzori et al., 2009 [2]	90 cm	$2.90 \times 10^{18}$ Nm	133°	47°
Cheloni et al., 2010 [39]	100 cm	$3.90 \times 10^{18}$ Nm	135°	50°
Cirella et al., 2009 [38]	110 cm	$3.50 \times 10^{18}$ Nm	133°	54°

Although triggered slip (up to 0.35 m) along the secondary low-angle fault does not greatly affect the coseismic surface displacements, the aftershocks distribution suggests two distinct faults [15,16]. Consequently, case 3 (Figure 10) which includes the low-angle secondary fault both matches the ground displacements and honors the aftershock pattern. Interestingly, the upper tip of the main fault has the same depth where Bigi et al. [15] placed a sub-horizontal fault. According to Bonini et al. [16] the upper tip of the L'Aquila rupture patch coincides with a remarkable discontinuity which can be interpreted as a thrust plane [16]. Aftershock alignments, focal mechanisms and receiver function analyses also highlight a lithological change associated with a discontinuity striking N 334° and dipping about 20° towards SW at 3–4 km depth [16].

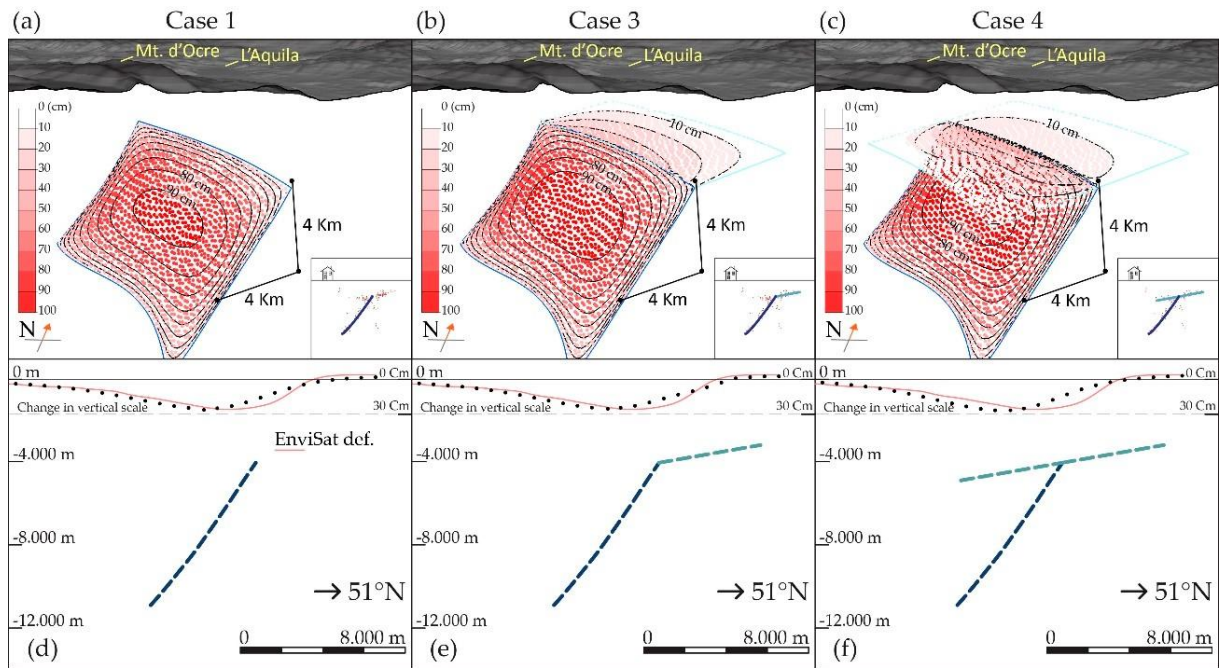


Figure 3.10. Slip distribution for (a) case 1, (b) case 3 and (c) case 4 with 3 MPa stress drop and 50 GPa Young's modulus. The cross-sections of (d–f) show the vertically exaggerated observed ground deformation (red line) [2] and the numerical models results (black dots) for our preferred cases.

## 3.6. Conclusions

We ran numerical models in order to execute a sensitivity analysis on five different 3D fault configurations by varying both stress drop and material stiffness. In our simulations, we also considered the potential influence of coseismic slip along a low angle inherited fault structure on ground deformation. According to our numerical models results, our preferred interpretation is that the L'Aquila earthquake activated a deep section of the Paganica fault causing only a little slip along faults near the Earth's surface. It also seems plausible that a blind normal fault triggered a local slip along a low-angle structure located around 3–4 km in depth.

The coseismic cracks are aligned along the surface expression of the Paganica fault; however, the model results from this study suggest that the slip of the 2009 L'Aquila earthquake remained mostly blind. Here we show that the best fits between DInSAR observation, and numerical simulation suggests that coseismic ground displacements do not seem to be a direct expression of fault slip at the Earth's surface in the L'Aquila 2009 earthquake. The numerical models' results also highlight (Figure 9) how fault geometry controls surface deformation pattern.

# References

1. Massonnet, D.; Rossi, M.; Carmona, C.; Adragna, F.; Peltzer, G.; Feigl, K.; Rabaute, T. The displacement field of the Landers earthquake mapped by radar interferometry. *Nature* 1993, 364, 138–142. [CrossRef]
2. Atzori, S.; Hunstad, I.; Chini, M.; Salvi, S.; Tolomei, C.; Bignami, C.; Stramondo, S.; Trasatti, E.; Antonioli, A.; Boschi, E. Finite fault inversion of DInSAR coseismic displacement of the 2009 L'Aquila earthquake (central Italy). *Geophys. Res. Lett.* 2009, 36. [CrossRef]
3. Chini, M.; Atzori, S.; Trasatti, E.; Bignami, C.; Kyriakopoulos, C.; Tolomei, C.; Stramondo, S. The May 12, 2008, (Mw 7.9) Sichuan Earthquake (China): Multiframed ALOS-PALSAR DInSAR analysis of coseismic deformation. *IEEE Geosci. Remote Sens. Lett.* 2010, 7, 266–270. [CrossRef]
4. Stramondo, S.; Cinti, F.R.; Dragoni, M.; Salvi, S.; Santini, S. The August 17, 1999 Izmit, Turkey, earthquake: Slip distribution from dislocation modeling of DInSAR and surface offset. *Ann. Geophys.* 2002, 45, 527–536.
5. Walters, R.J.; Elliott, J.R.; D'Agostino, N.; England, P.C.; Hunstad, I.; Jackson, J.A.; Parsons, B.; Phillips, R.J.; Roberts Edinburgh, G. The 2009 L'Aquila earthquake (central Italy): A source mechanism and implications for seismic hazard. *Geophys. Res. Lett.* 2009, 36, L15305. [CrossRef]
6. Wang, X.; Liu, G.; Yu, B.; Dai, K.; Zhang, R.; Chen, Q.; Li, Z. 3D coseismic deformations and source parameters of the 2010 Yushu earthquake (China) inferred from DInSAR and multiple-aperture InSAR measurements. *Remote Sens. Environ.* 2014, 152, 174–189. [CrossRef]
7. Trasatti, E.; Kyriakopoulos, C.; Chini, M. Finite element inversion of DInSAR data from the Mw 6.3 L'Aquila earthquake, 2009 (Italy). *Geophys. Res. Lett.* 2011, 38, L08306. [CrossRef]
8. Rovida, A.; Locati, M.; Camassi, R.; Lolli, B.; Gasperini, P. *CPT115, the 2015 Version of the Parametric Catalogue of Italian Earthquakes*; Istituto Nazionale di Geofisica e Vulcanologia: Rome, Italy, 2016; pp. 1–33.
9. Valoroso, L.; Chiaraluce, L.; Piccinini, D.; Di Stefano, R.; Schaff, D.; Waldhauser, F. Radiography of a normal fault system by 64,000 high-precision earthquake locations: The 2009 L'Aquila (central Italy) case study. *J. Geophys. Res. Solid Earth* 2013, 118, 1156–1176. [CrossRef]
10. Scognamiglio, L.; Tinti, E.; Michelini, A.; Dreger, D.S.; Cirella, A.; Cocco, M.; Mazza, S.; Piatanesi, A. Fast



- Determination of Moment Tensors and Rupture History: What Has Been Learned from the 6 April 2009 L'Aquila Earthquake Sequence. *Seismol. Res. Lett.* 2010, 81, 892–906. [CrossRef]
11. Serpelloni, E.; Anderlini, L.; Belardinelli, M.E. Fault geometry, coseismic-slip distribution and Coulomb stress change associated with the 2009 April 6,  $M_w$  6.3, L'Aquila earthquake from inversion of GPS displacements. *Geophys. J. Int.* 2012, 188, 473–489. [CrossRef]
  12. Boncio, P.; Pizzi, A.; Brozzetti, F.; Pomposo, G.; Lavecchia, G.; Di Naccio, D.; Ferrarini, F. Coseismic ground deformation of the 6 April 2009 L'Aquila earthquake (central Italy,  $M_w$ 6.3). *Geophys. Res. Lett.* 2010, 37, L06308. [CrossRef]
  13. Vannoli, P.; Burrato, P.; Fracassi, U.; Valensise, G. A fresh look at the seismotectonics of the Abruzzi (Central Apennines) following the 6 April 2009 L'Aquila earthquake ( $M_w$  6.3). *Ital. J. Geosci.* 2012, 131, 309–329.
  14. Lavecchia, G.; Ferrarini, F.; Brozzetti, F.; De Nardis, R.; Boncio, P.; Chiaraluce, L. From surface geology to aftershock analysis: Constraints on the geometry of the L'Aquila 2009 seismogenic fault system. *Ital. J. Geosci.* 2012, 131, 330–347.
  15. Bigi, S.; Casero, P.; Chiarabba, C.; Di Bucci, D. Contrasting surface active faults and deep seismogenic sources unveiled by the 2009 L'Aquila earthquake sequence (Italy). *Terra Nov.* 2013, 25, 21–29. [CrossRef]
  16. Bonini, L.; Di Bucci, D.; Toscani, G.; Seno, S.; Valensise, G. On the complexity of surface ruptures during normal faulting earthquakes: Excerpts from the 6 April 2009 L'Aquila (central Italy) earthquake ( $M_w$  6.3). *Solid Earth* 2014, 5, 389–408. [CrossRef]
  17. Castaldo, R.; de Nardis, R.; DeNovellis, V.; Ferrarini, F.; Lanari, R.; Lavecchia, G.; Pepe, S.; Solaro, G.; Tizzani, P. Coseismic Stress and Strain Field Changes Investigation Through 3-D Finite Element Modeling of DInSAR and GPS Measurements and Geological/Seismological Data: The L'Aquila (Italy) 2009 Earthquake Case Study. *J. Geophys. Res. Solid Earth* 2018, 123, 4193–4222. [CrossRef]
  18. Guerrieri, L.; Baer, G.; Hamiel, Y.; Amit, R.; Blumetti, A.M.; Comerci, V.; Di Manna, P.; Michetti, A.M.; Salamon, A.; Mushkin, A.; et al. InSAR data as a field guide for mapping minor earthquake surface ruptures: Ground displacements along the Paganica Fault during the 6 April 2009 L'Aquila earthquake. *J. Geophys. Res. Solid Earth* 2010, 115, B12331. [CrossRef]

19. Chiarabba, C.; Amato, A.; Anselmi, M.; Baccheschi, P.; Bianchi, I.; Cattaneo, M.; Cecere, G.; Chiaraluce, L.; Ciaccio, M.G.; De Gori, P.; et al. The 2009 L'Aquila (central Italy)  $M_w$ 6.3 earthquake: Main shock and aftershocks. *Geophys. Res. Lett.* 2009, *36*, L18308. [CrossRef]
20. Chiaraluce, L.; Valoroso, L.; Piccinini, D.; Di Stefano, R.; De Gori, P. The anatomy of the 2009 L'Aquila normal fault system (central Italy) imaged by high resolution foreshock and aftershock locations. *J. Geophys. Res. Solid Earth* 2011, *116*, B12311. [CrossRef]
21. Calamita, F.; Satolli, S.; Scisciani, V.; Eserstine, P.; Pace, P. Contrasting styles of fault reactivation in curved orogenic belts: Examples from the central Apennines (Italy). *Bull. Geol. Soc. Am.* 2011, *123*, 1097–1111. [CrossRef]
22. Di Domenico, A.; Bonini, L.; Calamita, F.; Toscani, G.; Galuppo, C.; Seno, S. Analogue modeling of positive inversion tectonics along differently oriented pre-thrusting normal faults: An application to the Central-Northern Apennines of Italy. *Bull. Geol. Soc. Am.* 2014, *126*, 943–955. [CrossRef]
23. Patacca, E.; Scandone, P. Post-Tortonian mountain building in the Apennines. The role of the passive sinking of a relic lithospheric slab. In *The Lithosphere in Italy*; Boriani, A., Bonafede, M., Piccardo, G.B., Vai, G.G., Eds.; Accademia Nazionale dei Lincei: Roma, Italy, 1989; pp. 157–176.
24. Barchi, M.; De Feyter, A.; Magnani, M.B.; Minelli, G.; Pialli, G. The structural style of the Umbria-Marche fold and thrust belt. *Mem. Soc. Geol. It.* 1998, *52*, 557–578.
25. Barba, S.; Basili, R. Analysis of seismological and geological observations for moderate-size earthquakes: The Colfiorito Fault System (Central Apennines, Italy). *Geophys. J. Int.* 2000, *141*, 241–252. [CrossRef]
26. Toscani, G.; Seno, S.; Fantoni, R.; Rogledi, S. Geometry and timing of deformation inside a structural arc: The case of the western Emilian folds (Northern Apennine front, Italy). *Boll. della Soc. Geol. Ital.* 2006, *125*, 59–65.
27. Cavinato, G.P.; Carusi, C.; Dall'asta, M.; Miccadei, E.; Piacentini, T. Sedimentary and tectonic evolution of Plio-Pleistocene alluvial and lacustrine deposits of Fucino Basin (central Italy). *Sediment. Geol.* 2002, *148*, 29–59. [CrossRef]
28. Patacca, E.; Scandone, P.; Di Luzio, E.; Cavinato, G.P.; Parotto, M. Structural architecture of the central Apennines: Interpretation of the CROP 11 seismic profile from the Adriatic coast to the orographic divide. *Tectonics* 2008, *27*. [CrossRef]

29. Tavarnelli, E.; Renda, P.; Pasqui, V.; Tramutoli, M. The effects of post-orogenic extension on different scales: An example from the Apennine-Maghrebide fold-and-thrust belt, SW Sicily. *Terra Nov.* 2003, 15, 1–7. [CrossRef]
30. Improta, L.; Villani, F.; Bruno, P.P.; Castiello, A.; De Rosa, D.; Varriale, F.; Punzo, M.; Brunori, C.A.; Civico, R.; Pierdominici, S.; et al. High-resolution controlled-source seismic tomography across the Middle Aterno basin in the epicentral area of the 2009, Mw 6.3, L'Aquila earthquake (central Apennines, Italy). *Ital. J. Geosci.* 2012, 131, 373–388.
31. D'Agostino, N.; Mantenuto, S.; D'Anastasio, E.; Giuliani, R.; Mattone, M.; Calcaterra, S.; Gambino, P.; Bonci, L. Evidence for localized active extension in the central Apennines (Italy) from global positioning system observations. *Geology* 2011, 39, 291–294. [CrossRef]
32. Anderson, H.; Jackson, J. Active tectonics of the Adriatic Region. *Geophys. J. R. Astron. Soc.* 1987, 91, 937–983. [CrossRef]
33. Roberts, G.P.; Michetti, A.M.; Cowie, P.; Morewood, N.C.; Papanikolaou, I. Fault slip-rate variations during crustal-scale strain localisation, central Italy. *Geophys. Res. Lett.* 2002, 29, 9-1–9-4. [CrossRef]
34. Vezzani, L.; Festa, A.; Ghisetti, F. Geological-structural map of the Central-Southern Apennines (Italy), 1:250,000 scale. Available online: <http://hdl.handle.net/2318/59925> (accessed on 24 August 2019).
35. Margheriti, L.; Chiaraluce, L.; Voisin, C.; Cultrera, G.; Govoni, A.; Moretti, M.; Bordoni, P.; Luzi, L.; Azzara, R.; Valoroso, L.; et al. Rapid response seismic networks in Europe: Lessons learnt from the L'Aquila earthquake emergency. *Ann. Geophys.* 2011, 54, 392–399.
36. Stucchi, M.; Camassi, R.; Rovida, A.; Locati, M.; Ercolani, E.; Meletti, C.; Migliavacca, P.; Bernardini, F.; Azzara, R. DBMI04, il database delle osservazioni macrosismiche dei terremoti italiani utilizzate per la compilazione del catalogo parametrico CPTI04. *Quad. Geofis.* 2007, 49, 1–38.
37. Anzidei, M.; Boschi, E.; Cannelli, V.; Devoti, R.; Esposito, A.; Galvani, A.; Melini, D.; Pietrantonio, G.; Riguzzi, F.; Sepe, V.; et al. Coseismic deformation of the destructive April 6, 2009 L'Aquila earthquake (central Italy) from GPS data. *Geophys. Res. Lett.* 2009, 36, L17307. [CrossRef]
38. Cirella, A.; Piatanesi, A.; Cocco, M.; Tinti, E.; Scognamiglio, L.; Michelini, A.; Lomax, A.; Boschi, E. Rupture history of the 2009 L'Aquila (Italy) earthquake from non-linear joint inversion of strong motion and GPS data. *Geophys. Res. Lett.* 2009, 36, L19304. [CrossRef]

39. Cheloni, D.; D'Agostino, N.; D'Anastasio, E.; Avallone, A.; Mantenuto, S.; Giuliani, R.; Mattone, M.; Calcaterra, S.; Gambino, P.; Dominici, D.; et al. Coseismic and initial post-seismic slip of the 2009 Mw 6.3 L'Aquila earthquake, Italy, from GPS measurements. *Geophys. J. Int.* 2010, *181*, 1539–1546.
40. Emergeo Working Group. *Rilievi Geologici di Terreno Effettuati Nell'area Epicentrale Della Sequenza Sismica Dell'aquilano del 6 Aprile 2009*; Istituto Nazionale di Geofisica e Vulcanologia: Rome, Italy, 2009; pp. 1–59.
41. Fujiwara, S.; Yurai, H.; Kobayashi, T.; Morishita, Y.; Nakano, T.; Miyahara, B.; Nakai, H.; Miura, Y.; Ueshiba, H.; Kakiage, Y.; et al. Small-displacement linear surface ruptures of the 2016 Kumamoto earthquake sequence detected by ALOS-2 SAR interferometry 4. Seismology 2016 Kumamoto earthquake sequence and its impact on earthquake science and hazard assessment Manabu Hashimoto, Martha Savage, Takuya Nishimura and Haruo Horikawa. *Earth Planets Sp.* 2016, *68*, 160.
42. Bagnaia, R.; D'Epifanio, A.; Sylos Labini, S. Aquila and Subequan basins: an example of Quaternary evolution in central Apennines, Italy. *Quat. Nova.* 1992, *II*, 187–209.
43. Vittori, E.; di Manna, P.; Blumetti, A.M.; Comerci, V.; Guerrieri, L.; Esposito, E.; Michetti, A.M.; Porfido, S.; Piccardi, L.; Roberts, G.P.; et al. Surface faulting of the 6 April 2009 mw 6.3 L'Aquila earthquake in central Italy. *Bull. Seismol. Soc. Am.* 2011, *101*, 1507–1530. [CrossRef]
44. Albano, M.; Barba, S.; Saroli, M.; Moro, M.; Malvarosa, F.; Costantini, M.; Bignami, C.; Stramondo, S. Gravity-driven postseismic deformation following the Mw 6.3 2009 L'Aquila (Italy) earthquake. *Sci. Rep.* 2015, *5*, 16558. [CrossRef]
45. Chiaraluce, L. Unravelling the complexity of Apenninic extensional fault systems: A review of the 2009 L'Aquila earthquake (Central Apennines, Italy). *J. Struct. Geol.* 2012, *42*, 2–18. [CrossRef]
46. Falcucci, E.; Gori, S.; Peronace, E.; Fubelli, G.; Moro, M.; Saroli, M.; Giaccio, B.; Messina, P.; Naso, G.; Scardia, G.; et al. The Paganica Fault and Surface Coseismic Ruptures Caused by the 6 April 2009 Earthquake (L'Aquila, Central Italy). *Seismol. Res. Lett.* 2009, *80*, 940–950. [CrossRef]

47. Thomas, A.L. Poly3D: A Three-dimensional, Polygonal Element, Displacement Discontinuity Boundary Element Computer Program with Applications to Fractures, Faults, and Cavities in the Earth's crust. Ph.D. Thesis, Stanford University, Stanford, CA, USA, June 1993.
48. Maerten, L.; Willemsse, E.J.M.; Pollard, D.D.; Rawnsley, K. Slip distributions on intersecting normal faults.  
*J. Struct. Geol.* 1999, *21*, 259–272. [CrossRef]
49. Willemsse, E.J.M.; Pollard, D.D.; Aydin, A. Three-dimensional analyses of slip distributions on normal fault arrays with consequences for fault scaling. *J. Struct. Geol.* 1996, *18*, 295–309. [CrossRef]
50. Crider, J.G.; Pollard, D.D. Fault linkage: Three-dimensional mechanical interaction between echelon normal faults. *J. Geophys. Res. Solid Earth* 1998, *103*, 24373–24391. [CrossRef]
51. Madden, E.H.; Pollard, D.D. Integration of surface slip and aftershocks to constrain the 3D structure of faults involved in the M 7.3 Landers earthquake, Southern California. *Bull. Seismol. Soc. Am.* 2012, *102*, 321–342. [CrossRef]
52. Fattaruso, L.A.; Cooke, M.L.; Dorsey, R.J. Sensitivity of uplift patterns to dip of the San Andreas fault in the Coachella Valley, California. *Geosphere* 2014, *10*, 1235–1246. [CrossRef]
53. Dorsett, J.H.; Madden, E.H.; Marshall, S.T.; Cooke, M.L. Mechanical Models Suggest Fault Linkage through the Imperial Valley, California, USA. *Bull. Seismol. Soc. Am.* 2019. [CrossRef]
54. Yoffe, E.H. The angular dislocation. *Philos. Mag.* 1960, *5*, 161–175. [CrossRef]
55. Comninou, M.; Dundurs, J. The angular dislocation in a half space. *J. Elast.* 1975, *5*, 203–216. [CrossRef]
56. Brown, R.L. A dislocation approach to plate interaction. Ph.D. Thesis, Massachusetts Institute of Technology, Department of Earth and Planetary Sciences, Cambridge, MA, USA, August 1975.
57. Jeyakumar, M. Modeling slip zones with triangular dislocation elements. *Bull. Seismol. Soc. America* 1992, *82*, 2153–2169.
58. Maerten, F.; Resor, P.; Pollard, D.; Maerten, L. Inverting for slip on three-dimensional fault surfaces using angular dislocations. *Bull. Seismol. Soc. Am.* 2005, *95*, 1654–1665. [CrossRef]
59. Cheng, L.W.; Lee, J.C.; Hu, J.C.; Chen, H.Y. Coseismic and postseismic slip distribution of the 2003 Mw = 6.5 Chengkung earthquake in eastern Taiwan: Elastic modeling from inversion of GPS data. *Tectonophysics* 2009,

466, 335–343. [CrossRef]

60. Bonini, L.; Basili, R.; Toscani, G.; Burrato, P.; Seno, S.; Valensise, G. The role of pre-existing discontinuities in the development of extensional faults: An analog modeling perspective. *J. Struct. Geol.* 2015, *74*, 145–158. [CrossRef]
61. Pacor, F.; Spallarossa, D.; Oth, A.; Luzi, L.; Puglia, R.; Cantore, L.; Mercuri, A.; D'Amico, M.; Bindi, D. Spectral models for ground motion prediction in the L'Aquila region (central Italy): Evidence for stress-drop dependence on magnitude and depth. *Geophys. J. Int.* 2016, *204*, 697–718. [CrossRef]
62. Yasar, E.; Erdogan, Y. Correlating sound velocity with the density, compressive strength and Young's modulus of carbonate rocks. *Int. J. Rock Mech. Min. Sci.* 2004, *41*, 871–875. [CrossRef]
63. Allmann, B.P.; Shearer, P.M. Global variations of stress drop for moderate to large earthquakes. *J. Geophys. Res. Solid Earth* 2009, *114*, B01310. [CrossRef]
64. Salazar-Mora, C.A.; Huisman, R.S.; Fossen, H.; Egydio-Silva, M. The Wilson Cycle and Effects of Tectonic Structural Inheritance on Rifted Passive Margin Formation. *Tectonics* 2018, *37*, 3085–3101. [CrossRef]
65. Wilkinson, M.; McCaffrey, K.J.W.; Roberts, G.; Cowie, P.A.; Phillips, R.J.; Michetti, A.M.; Vittori, E.; Guerrieri, L.; Blumetti, A.M.; Bubeck, A.; et al. Partitioned postseismic deformation associated with the 2009 Mw 6.3 L'Aquila earthquake surface rupture measured using a terrestrial laser scanner. *Geophys. Res. Lett.* 2010, *37*. [CrossRef]

---

## Chapter 4. Slip inversion

# Coseismic slip inversion on nonplanar fault: the 2009 L'Aquila earthquake.

Yuri Panara <sup>1,\*</sup>, Giovanni Toscani <sup>1,3</sup>, Michele L. Cooke <sup>2</sup>, Silvio Seno <sup>1,3</sup> and Cesare Perotti <sup>1,3</sup>

<sup>1</sup> Department of Earth and Environmental Sciences, University of Pavia, Pavia I-27100, Italy

<sup>2</sup> Department of Geosciences, University of Massachusetts, Amherst, MA 01003, USA

<sup>3</sup> CRUST (Centro interUniversitario per l'analisi SismoTettonica tridimensionale con applicazioni territoriali), Pavia I-27100, Italy

\* Correspondence: [yuri.panara01@universitadipavia.it](mailto:yuri.panara01@universitadipavia.it)

The development of DInSAR technique and the increasing density in GPS stations network provide a large amount of data available for geologist and geophysicist for slip inversion models. Usually inversion models use planar rectangular surfaces to model fault ruptures, those assumptions could simplify the reconstructed slip distributions. In this chapter we are going to show the preliminary result on the inversion models we run during the PhD project. Chapter 3 described how different faults geometries were interpreted using aftershocks and coseismic cracks distribution. Those non-planar fault surfaces were used inside Poly3D software to reproduce the coseismic ground deformation observed after the 2009 L'Aquila main shock. This method proved to be reliable (Panara et al., 2019) to reproduce the DInSAR observed deformation (Atzori et al., 2009), however Poly3D also provided a slip path distribution on the tested fault surface. Despite the assumption involved, the models with a good correspondence between observed and predicted surface deformation also provide slip distribution, maximum slip amount and seismic moment consistent with previous published reconstructions (Atzori et al., 2009; Cirella et al., 2009; Cheloni et al., 2010). However, we tried to use a different approach using a Matlab code specifically designed to run slip inversion. This work was made possible using Trinvx a three-dimensional slip-inversion code provided by Prof. J. Loveless (Smith College, MA,

USA). As well of Poly3D, Trinvx is developed in a linear-elastic, homogeneous, isotropic, half-space. The inversion models were validate comparing the obtained seismic moment and the maximum slip value with previous published reconstructions. This models helps to better constrain the slip patch distribution on non-planar faults surface understanding how slip propagate toward Earth surface.

## 4.1. Introduction

The 2009 L'Aquila earthquake occurs on the Paganica fault, surface deformation involved an area of over 100 Km<sup>2</sup> (Emergeo Working Group 2009; Boncio et al., 2010, Atzori et al., 2009) inside the Central Apennines causing 306 casualties and major damage on the town of L'Aquila. The Apennines are the result of a composite history, several tectonic phases overlapped over a long geological time. In particular, the L'Aquila region was once part of African's passive margin, housing a large carbonate platform with a thick pelagic basin. This area was then involved in the Triassic-Jurassic rifting (Calamita et al., 2011; Di Domenica et al., 2014). From the Cretaceous up to the Middle Pleistocene the convergence between Africa and Europe lead to the formation of a thrust system with the related foreland basin toward the Adriatic Sea (Patacca et al., 1989; Toscani et al., 2006). Today the entire region is interested by normal faulting, Central Apennine has been affected in the last 2.5 Ma by SW-NE extension (Cavinato et al., 2002; Tavarnelli et al., 2003). The present extensional rate has been quantified in 2-3 mm/year (D'Agostino et al., 2011). The quaternary extensional phase causes the development of numerous high angle normal faults, and these faults drive the recent evolution of several intra-mountain sedimentary basins with sediment thickness up to 250 m underneath L'Aquila (Improta et al., 2012). Although normal fault along Apennines are mostly high-angle there are exceptions, for the seismic sequence of Central Italy 2016 the reactivation of a preexisting low-angle normal fault, likely related to a segment of the Sibillini Thrust has been proposed (Lavecchia et al., 2016; Chiaraluce et al., 2017; Cheloni et al., 2017).

Several studies were run about the 2009 L'Aquila earthquake, collecting multiple data information about the seismic sequence (Chiarabba et al., 2009; Chiaraluce et al., 2011;



Chiaraluce et al., 2012; Valoroso et al. 2013), focal mechanism (Scognamiglio et al., 2010), coseismic ground deformation (Atzori et al., 2009), coseismic surface crack (Emergeo Working Group, 2009; Boncio et al., 2010) and post-seismic deformation (Wilkinson et al., 2010). Those data were used to constrain several possible fault geometries (see Vannoli et al., 2012 for a review), despite that numerous question persist on the slip propagation toward the surface (Bigi et al., 2013; Bonini et al., 2014).

## 4.2. Methods

In this paper we executed the slip inversion on two different fault geometries reconstructed using aftershocks distribution (Valoroso et al., 2013) and coseismic surface faulting mapped after the mainshock (Boncio et al., 2009). We run slip inversion over three different fault configuration in order to observe slip distribution on different reliable possibilities. This approach was made necessary because many uncertainties persist about slip upward propagation toward ground surface and on the importance of coseismic cracks (Emergeo Working Group, 2009; Boncio et al., 2010). All the faults were rebuilt autonomously in the way described by Panara et al. (2019), according to previous published fault setting (Boncio et al., 2010, Atzori et al., 2009; Lavecchia et al., 2012; Bigi et al., 2013; Bonini et al., 2014). The two tested configuration were (Figure 4.1):

- Case 1, a blind fault (Bigi et al., 2013; Bonini et al., 2014; Panara et al., 2019);
- Case 2, a fault outcropping on the Earth surface (Boncio et al., 2010; Lavecchia et al., 2012).

The main fault's features are summarized in Table 4.1, the proposed normal fault configuration striking 130°-135°N, dipping 50°-55° toward SW and the lower tip is placed 12 Km below the surface, these parameters are in accordance with most of the proposed reconstructions (see Vannoli et al., 2012 for a review).

Table 4.1. Summary of the geometrics features of the teste fault.

Case	Dept max.	Dept min	Dip	Strike	Area
Case 1	12 km	4 Km	50 – 55 °	130 – 135 °N	171 Km <sup>2</sup>
Case 2	12 Km	0 Km	50 – 55 °	130 – 135 °N	264 Km <sup>2</sup>

Taking advantage of the modern DInSAR observation and using the dense permanent and temporary GPS network (Anzidei et al., 2008; Anzidei et al., 2009) set up in the central section of the Apennines (Anzidei et al., 2005) after the 1997 Marche-Umbria seismic sequence several multiple inversion were conducted. The reconstructions of the depth geometry of the Paganica fault responsible for the L'Aquila earthquake were based on GPS data, DInSAR observation or using both (Anzidei et al., 2008; Atzori et al., 2009).

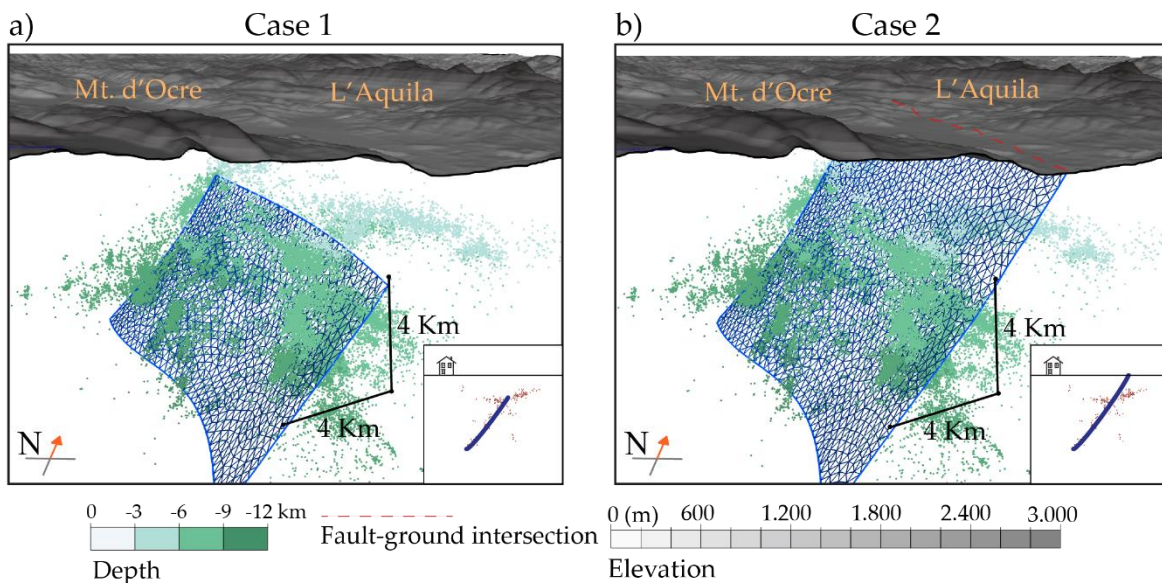


Figure 4.1. 3D view of the two fault configurations of the numerical models with (in green) the aftershock cloud. (a) Case 1: blind normal fault; (b) Case 2: normal fault reaches the ground surface.

The coseismic ground deformation has been determined using the DInSAR (Differential SAR Interferometry) technique on Envisat images (Atzori et al., 2009). In this work we used the 01/02/2009 - 12/04/2009 pair acquired from descending orbit, with a 148 perpendicular

baseline and a  $23^\circ$  right look angle (Atzori et al., 2009). The DInSAR deformation was integrated with GPS data (Atzori et al., 2009). The observed deformation occurred in an area of about  $100 \text{ Km}^2$  with a maximum measured subsidence of 29 Cm and an uplift of 7 Cm (Atzori et al., 2009). The DInSAR analysis did not show a sharp change in displacement, the minimum and the maximum deformation are separate by 5 Km distance (Atzori et al., 2009). Because of this, several of the best fit DInSAR inversion and reconstructions have a very little coseismic slip near ground surface (Walters et al., 2009) or have proposed a blind fault solution (Bigi et al., 2013; Bonini et al., 2014; Panara et al., 2019).

The available surface deformation dataset was composed by over 2.000 deformation point (Figure 4.2 a) provide by Atzori et al., (2009), for this study we used 75 point (Figure 4.2 b). The number and distribution of point are accurate enough to obtain an accurate slip inversion.

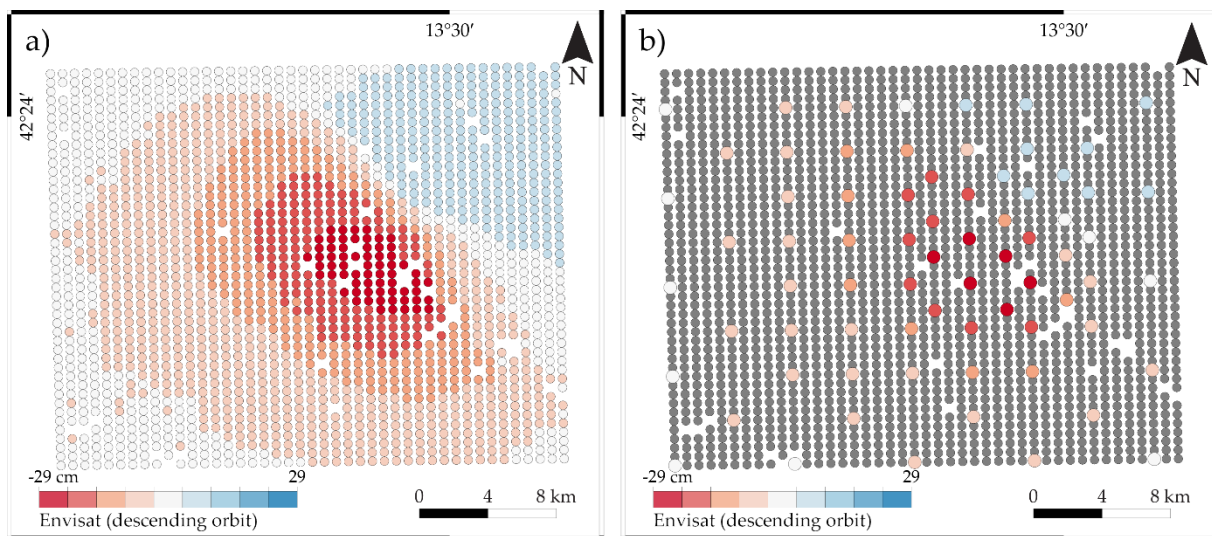


Figure 4.2. This is a figure: (a) The 2.000 composing the original observation grid provided by Atzori et al., (2009); (b) The grid used for inversion models. It is possible to notice how the point of maximum subsidence is separated by the point of maximum uplift by a distance of over 5 Km. The gentle gradient between the two point seems to exclude a direct slip propagation toward Earth's surface for L'Aquila earthquake.

Despite the resampling, the number of points on the grid provides an adequate reference, points are present over the entire deformed area. The points sample the area of

maximum subsidence and maximum uplift. Moreover, there are points at the edge of the area where the deformation is exhausted. The mesh size of the fault surfaces is 500 meters. Such a dense mesh can increase the quality of the slip inversion but can also increase the computation time. The main reason because we decided to keep the same meshes was to make a comparison between the slip prediction resulting from Poly3D software and the solutions obtained with Trinix code. Both solutions are reliable for this earthquake providing about  $10^{18}$  Nm seismic moment. However, differences between the solutions are prominent. Poly3D provide a homogeneous elliptical distribution of the slip on ground surface only according to the applied stress drop and host rock stiffness (Panara et al., 2019). Trinix provide a solution according to the surface deformation pattern and on fault geometry. Trinix seems to be more accurate and realistic, with a slip pattern that is not homogenously distributed on fault surface.

### 4.3 Results

The slip parameter resulting from the inversion are summarized in Table 4.2. We assumed a host rock rigidity of 30 Gpa (Atzori et al., 2009), the three solutions have a seismic moment in the order of size of  $10^{18}$  Nm, corresponding to a moment magnitude of 6.3 in agreement with previous proposed reconstruction (Atzori et al., 2009; Anzidei et al., 2009; Cheloni et al., 2010; Cirella et al., 2019; Guerrieri et al., 2010; Panara et al., 2019). The non-planar fault geometries have strike values between  $130^\circ$  and  $135^\circ$ N, while the dip vary between  $50^\circ$  and  $55^\circ$  (see Vannoli et al., 2012 for a review).

Table 4.1. Summary of the slip inversions results.

Case	Area [m <sup>2</sup> ]	Shear Mod. [Pa]	Average Slip [m]	Slip Max [m]	Seismic Moment [Nm]
Case 1	171 X 10 <sup>6</sup>	30 X 10 <sup>9</sup>	0.38	1.3	2.0 X 10 <sup>18</sup>
Case 2	264 X 10 <sup>6</sup>	30 X 10 <sup>9</sup>	0.40	1.5	3.5 X 10 <sup>18</sup>

$$M_0 = \mu AD$$

$M_0$ =Seismic moment [Nm],  $\mu$ = Shear modulus [Pa],  $A$ =area [m<sup>2</sup>],  $D$ =average slip [m]

All the three tested fault geometries have the lower tip placed at 12 km depth, the lateral length is 18 Km. The blind case solution has the upper tip placed 4 Km below the surface, while case 2 daylight ground surface. The position, size and orientation of the fault plane derive from the reconstruction run by Panara et al. (2019) and have a good correspondence with the relocate aftershock (Valoroso et al., 2013) and the observed coseismic cracks (Boncio et al., 2010). We force a normal slip behavior in agreement with the focal mechanism (Scognamiglio et al., 2010).

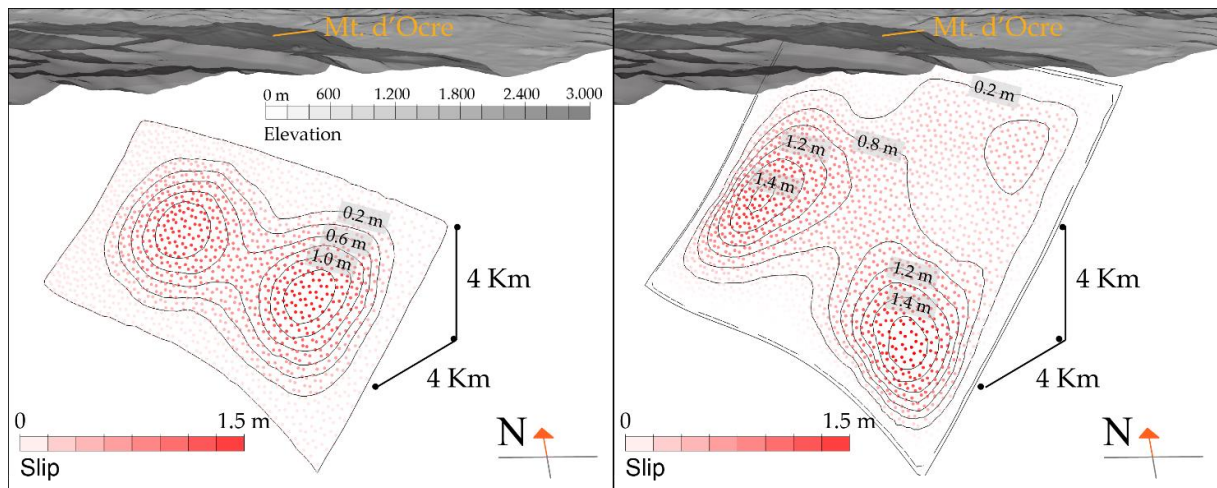


Figure 4.3. Slip distribution resulting from inversion models.

For the first model, we obtained maximum slip values of 1.3 meters. The slip is not distributed evenly along the fault but is concentrated in two spots located about 6 km deep. The second model has a maximum slip of 1.5 m, the maximum slip is also observed in this case 6-7 km in depth. Also, for the second case the slip is not distributed uniformly throughout the fault area but is divided into two main areas. It is interesting to note that in case 2, the outcropping fault, the slip concentrates mainly in depth. Above 3 km depth the slip is greatly reduced. The reconstructions proposed in the literature are similar to those obtained from this models. The seismic moment calculated for these two cases is 2 and 3.5  $\times 10^{18}$  Nm. The previously proposed reconstructions estimate a seismic moment between 2.7 (Atzori et al., 2009) and 3.4  $\times 10^{18}$  Nm (CMT inversion). While the reconstruction of the maximum slip, especially for case 2, seems to be too high. The reconstructions proposed in the literature (Vannoli et al., 2012) propose maximum slip values of about one meter, up to 1.2 m (Trasatti et al., 2012)

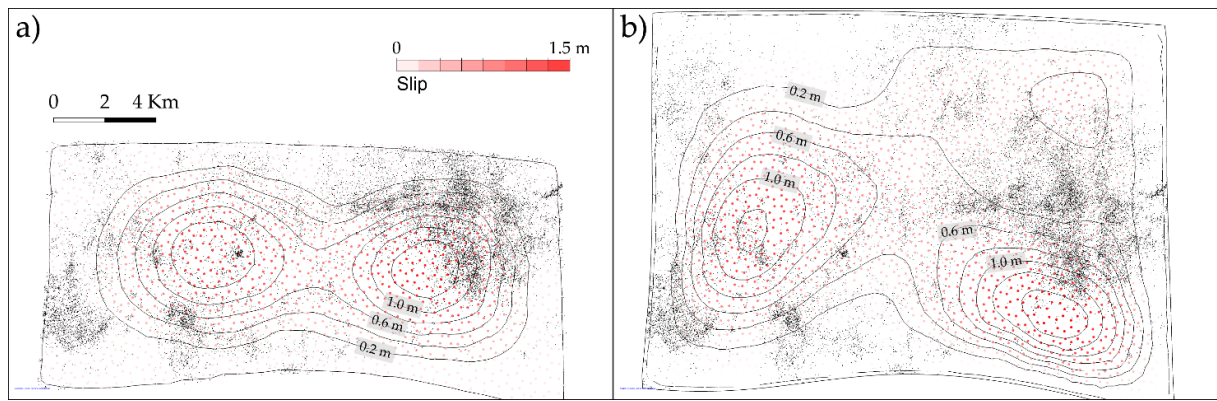


Figure 4.4. Slip distribution compared to aftershock distribution.

Aftershocks distribution was used to interpret the faults (Chapter 3), however aftershocks were not included in the inversion model. From the comparison (Figure 4.4) it is possible to observe how the aftershocks seem to concentrate mainly outside the areas of maximum slip (Di Stefano et al., 2011; Cirella et al., 2012; Valoroso et al., 2013).

## 4.4 Conclusions

We determined the co-seismic slip patch after L'Aquila earthquake for two different non-planar fault surfaces (Panara et al., 2019) inverting the Envisat DInSAR observed coseismic deformation (Atzori et al., 2009). We tested different two different cases: blind and outcropping fault. Our reconstructions show maximum slip and seismic moment in agreement with the result of older reconstructions (Anzidei et al., 2009; Atzori et al., 2009, Vannoli et al., 2012). It is interesting to note that in both cases the slip distribution was concentrated at a depth (Bigi et al., 2013; Bonini et al., 2014; Panara et al., 2019).



## 4.5 References

1. Anzidei, M., P. Baldi, A. Pesci, A. Esposito, A. Galvani, F. Loddo, P. Cristofolletti, A. Massucci, and S. Del Mese (2005), Geodetic deformation across the Central Apennines from GPS data in the time span 1999– 2003, *Ann. Geophys.*, 48(2), 259–271.
2. Anzidei, M., P. Baldi, A. Pesci, S. Del Mese, A. Esposito, A. Galvani, F. Loddo, A. Massucci, and P. Cristofolletti (2008), La rete geodetica GPS dell'Appennino Centrale CA-GeoNet, Quaderni Geofis. 54, Ist. Naz. di Geofis. e Vulcanol., Rome.
3. Atzori, S.; Hunstad, I.; Chini, M.; Salvi, S.; Tolomei, C.; Bignami, C.; Stramondo, S.; Trasatti, E.; Antonioli, A.; Boschi, E. Finite fault inversion of DInSAR coseismic displacement of the 2009 L'Aquila earthquake (central Italy). *Geophys. Res. Lett.* 2009, 36, doi:10.1029/2009GL039293
4. Bigi, S.; Casero, P.; Chiarabba, C.; Di Bucci, D. Contrasting surface active faults and deep seismogenic sources unveiled by the 2009 L'Aquila earthquake sequence (Italy). *Terra Nov.* 2013, 25, 21–29.
5. Boncio, P.; Pizzi, A.; Brozzetti, F.; Pomposo, G.; Lavecchia, G.; Di Naccio, D.; Ferrarini, F. Coseismic ground deformation of the 6 April 2009 L'Aquila earthquake (central Italy,  $M_w > 6.3$ ). *Geophys. Res. Lett.* 2010, 37, L06308.
6. Bonini, L.; Di Bucci, D.; Toscani, G.; Seno, S.; Valensise, G. On the complexity of surface ruptures during normal faulting earthquakes: Excerpts from the 6 April 2009 L'Aquila (central Italy) earthquake ( $M_w 6.3$ ). *Solid Earth* 2014, 5, 389–408.
7. Calamita, F.; Satolli, S.; Scisciani, V.; Eserstine, P.; Pace, P. Contrasting styles of fault reactivation in curved orogenic belts: Examples from the central Apennines (Italy). *Bull. Geol. Soc. Am.* 2011, 123, 1097–1111.
8. Cavinato, G.P.; Carusi, C.; Dall'asta, M.; Miccadei, E.; Piacentini, T. Sedimentary and tectonic evolution of Plio-Pleistocene alluvial and lacustrine deposits of Fucino Basin (central Italy). *Sediment. Geol.* 2002, 148, 29–59.
9. Cheloni, D.; D'Agostino, N.; D'Anastasio, E.; Avallone, A.; Mantenuto, S.; Giuliani, R.; Mattone, M.; Calcaterra, S.; Gambino, P.; Dominici, D.; et al. Coseismic and initial



- post-seismic slip of the 2009 Mw 6.3 L'Aquila earthquake, Italy, from GPS measurements. *Geophys. J. Int.* 2010, *181*, 1539–1546.
10. Cheloni, D.; De Novellis, V.; Albano, M.; Antonioli, A.; Anzidei, M.; Atzori, S.; Avallone, A.; Bignami, C.; Bonano, M.; Calcaterra, S.; et al. Geodetic model of the 2016 Central Italy earthquake sequence inferred from InSAR and GPS data. *Geophys. Res. Lett.* 2017, *44*, 6778–6787.
  11. Chiarabba, C.; Amato, A.; Anselmi, M.; Baccheschi, P.; Bianchi, I.; Cattaneo, M.; Cecere, G.; Chiaraluce, L.; Ciaccio, M.G.; De Gori, P.; et al. The 2009 L'Aquila (central Italy) M<sub>w</sub>6.3 earthquake: Main shock and aftershocks. *Geophys. Res. Lett.* 2009, *36*, L18308.
  12. Chiaraluce, L.; Valoroso, L.; Piccinini, D.; Di Stefano, R.; De Gori, P. The anatomy of the 2009 L'Aquila normal fault system (central Italy) imaged by high resolution foreshock and aftershock locations. *J. Geophys. Res. Solid Earth* 2011, *116*, B12311.
  13. Chiaraluce, L. Unravelling the complexity of Apenninic extensional fault systems: A review of the 2009 L'Aquila earthquake (Central Apennines, Italy). *J. Struct. Geol.* 2012, *42*, 2–18.
  14. Chiaraluce, L.; Di Stefano, R.; Tinti, E.; Scognamiglio, L.; Michele, M.; Casarotti, E.; Cattaneo, M.; De Gori, P.; Chiarabba, C.; Monachesi, G.; et al. The 2016 central Italy seismic sequence: A first look at the mainshocks, aftershocks, and source models. *Seismol. Res. Lett.* 2017, *88*, 757–771.
  15. Cirella, A.; Piatanesi, A.; Cocco, M.; Tinti, E.; Scognamiglio, L.; Michelini, A.; Lomax, A.; Boschi, E. Rupture history of the 2009 L'Aquila (Italy) earthquake from non-linear joint inversion of strong motion and GPS data. *Geophys. Res. Lett.* 2009, *36*, L19304.
  16. D'Agostino, N.; Mantenuto, S.; D'Anastasio, E.; Giuliani, R.; Mattone, M.; Calcaterra, S.; Gambino, P.; Bonci, L. Evidence for localized active extension in the central Apennines (Italy) from global positioning system observations. *Geology* 2011, *39*, 291–294.
  17. Di Domenica, A.; Bonini, L.; Calamita, F.; Toscani, G.; Galuppo, C.; Seno, S. Analogue modeling of positive inversion tectonics along differently oriented pre-thrusting

- normal faults: An application to the Central-Northern Apennines of Italy. *Bull. Geol. Soc. Am.* 2014, 126, 943–955.
18. Di Stefano, R.; Chiarabba, C.; Chiaraluce, L.; Cocco, M.; De Gori, P.; Piccinini, D.; Valoroso, L. Fault zone properties affecting the rupture evolution of the 2009 (M w 6.1) L'Aquila earthquake (central Italy): Insights from seismic tomography. *Geophys. Res. Lett.* 2011.
  19. Emergeo Working Group. *Rilievi Geologici di Terreno Effettuati Nell'area Epicentrale Della Sequenza Sismica Dell'aquilano del 6 Aprile 2009*. Istituto Nazionale di Geofisica e Vulcanologia: Rome, Italy. 2009; pp. 1–59
  20. Guerrieri, L.; Baer, G.; Hamiel, Y.; Amit, R.; Blumetti, A.M.; Comerci, V.; Di Manna, P.; Michetti, A.M.; Salamon, A.; Mushkin, A.; et al. InSAR data as a field guide for mapping minor earthquake surface ruptures: Ground displacements along the Paganica Fault during the 6 April 2009 L'Aquila earthquake. *J. Geophys. Res. Solid Earth* 2010, 115, B12331.
  21. Improta, L.; Villani, F.; Bruno, P.P.; Castiello, A.; Rosa, D. De; Varriale, F.; Punzo, M.; Brunori, C.A.; Civico, R.; Pierdominici, S.; et al. High-resolution controlled-source seismic tomography across the Middle Aterno basin in the epicentral area of the 2009, Mw 6.3, L'Aquila earthquake (central Apennines, Italy). *Ital. J. Geosci.* 2012, 131, 373–388.
  22. Lavecchia, G.; Ferrarini, F.; Brozzetti, F.; Nardis, R. De; Boncio, P.; Chiaraluce, L. From surface geology to aftershock analysis: Constraints on the geometry of the L'Aquila 2009 seismogenic fault system. *Ital. J. Geosci.* 2012, 131, 330–347.
  23. Lavecchia, G.; Castaldo, R.; de Nardis, R.; De Novellis, V.; Ferrarini, F.; Pepe, S.; Brozzetti, F.; Solaro, G.; Cirillo, D.; Bonano, M.; et al. Ground deformation and source geometry of the 24 August 2016 Amatrice earthquake (Central Italy) investigated through analytical and numerical modeling of DInSAR measurements and structural-geological data. *Geophys. Res. Lett.* 2016, 43, 12,389–12,398.

24. Panara; Toscani; Cooke; Seno; Perotti Coseismic Ground Deformation Reproduced through Numerical Modeling: A Parameter Sensitivity Analysis. *Geosciences* 2019, 9, 370.
25. Patacca, E.; Scandone, P. Post-Tortonian mountain building in the Apennines. The role of the passive sinking of a relic lithospheric slab. In *The Lithosphere in Italy*; Boriani, A., Bonafede, M., Piccardo, G. B., Vai, G. G., Eds.; Accademia Nazionale dei Lincei: Roma, Italy, 1989; pp. 157–176.
26. Scognamiglio, L.; Tinti, E.; Michelini, A.; Dreger, D.S.; Cirella, A.; Cocco, M.; Mazza, S.; Piatanesi, A. Fast Determination of Moment Tensors and Rupture History: What Has Been Learned from the 6 April 2009 L'Aquila Earthquake Sequence. *Seismol. Res. Lett.* 2010, 81, 892–906.
27. Tavarnelli, E.; Renda, P.; Pasqui, V.; Tramutoli, M. The effects of post-orogenic extension on different scales: An example from the Apennine-Maghrebide fold-and-thrust belt, SW Sicily. *Terra Nov.* 2003, 15, 1–7.
28. Toscani, G.; Seno, S.; Fantoni, R.; Rogledi, S. Geometry and timing of deformation inside a structural arc: The case of the western Emilian folds (Northern Apennine front, Italy). *Boll. della Soc. Geol. Ital.* 2006, 125, 59–65.
29. Trasatti, E.; Kyriakopoulos, C.; Chini, M. Finite element inversion of DInSAR data from the Mw 6.3 L'Aquila earthquake, 2009 (Italy). *Geophys. Res. Lett.* 2011, 38, L08306.
30. Valoroso, L.; Chiaraluce, L.; Piccinini, D.; Di Stefano, R.; Schaff, D.; Waldhauser, F. Radiography of a normal fault system by 64,000 high-precision earthquake locations: The 2009 L'Aquila (central Italy) case study. *J. Geophys. Res. Solid Earth* 2013, 118, 1156–1176.
31. Vannoli, P.; Burrato, P.; Fracassi, U.; Valensise, G. A fresh look at the seismotectonics of the Abruzzi (Central Apennines) following the 6 April 2009 L'Aquila earthquake (Mw 6.3). *Ital. J. Geosci.* 2012, 131, 309–329.
32. Walters, R.J.; Elliott, J.R.; D'Agostino, N.; England, P.C.; Hunstad, I.; Jackson, J.A.; Parsons, B.; Phillips, R.J.; Roberts Edinburgh, G. The 2009 L'Aquila earthquake

(central Italy): A source mechanism and implications for seismic hazard. *Geophys. Res. Lett.* 2009, 36, L15305.

33. Wilkinson, M.; McCaffrey, K.J.W.; Roberts, G.; Cowie, P.A.; Phillips, R.J.; Michetti, A.M.; Vittori, E.; Guerrieri, L.; Blumetti, A.M.; Bubeck, A.; et al. Partitioned postseismic deformation associated with the 2009 Mw 6.3 L'Aquila earthquake surface rupture measured using a terrestrial laser scanner. *Geophys. Res. Lett.* 2010, 37, doi:10.1029/2010GL043099.

## 5. General results & conclusions

The aim of this thesis work was to investigate the relationship between normal faults and surface deformation. These kind of investigations can have numerous applicative and theoretical consequences. The main problem is that, while it is always possible to observe and measure ground deformation, the deep geometrical configuration of the fault is not always known. From what are the ground evidences (for example, a coseismic deformation, ground crack and ruptures, fault's traces) it is possible to reconstruct the position and the geometry of the fault with indirect investigation. Over this PhD project we investigated the topic with a multidisciplinary approach. Parallel to the main work, we have also perfected methodologies that will be applied in the future study cases. The acquisition of new knowledge and technique (Digital Photogrammetry) within the analog modeling laboratory of the University of Pavia is certainly a result of great importance.

During the first year we made a series of analogue models using dry quartz sand. These models made it possible to constrain the ground deformation to the geometrical features of an initial buried fault. This ideal case allowed us to constrain the surface deformation with the depth fault geometry. It has been shown that the surface deformation is directly proportional to the depth of burial and to the width of the fault. While it decreases with the reduction of the slip on the fault plane. Digital photogrammetry has proved to be a powerful tool for this kind of investigation. The use of a large number of high-resolution pictures combined with the use of a Python code has enabled a largely automatic procedure to be developed. The resolution, the number and the types of data obtainable are far greater than the previously used structured light. This know-how is an important tool that will be made available for future analog modeling studies.

About the natural case we reproduce the coseismic deformation observed after the L'Aquila 2009 earthquake. In an area without direct depth underground investigation it represents the only information available to refer to. During this work it was possible, starting from a robust dataset composed of geological and geophysical data, to reconstruct a reliable geological model. Based on the published reconstructions proposed by different authors, five fault's geometries, seven stress drop and seven host rock stiffness values

(Young's Modulus) were tested inside the models. Testing a wide range of possibilities, based on previously published works, an impartial sensitivity analysis of the results was carried out. From this analysis we have obtained three main results. First, we have seen how the cases in which the fault reaches the surface it is not possible to reproduce the coseismic deformation observed after the earthquake of April 9, 2009. The best results have always been obtained by testing a blind fault. This result is consistent with the field observations, with the observed coseismic deformation and also considering the general geological framework. The presence of active normal faults and old thrusts inherited in the same area let imagine a complex situation. The new faults currently active during their development have had to interact with existing mechanical discontinuities. These discontinuities can represent an important obstacle, capable in theory of totally blocking their propagation towards the surface. The second result obtained is that from the analysis of the results it was possible to quantify the relative importance that the three parameters tested had on the result. Although it is always important to rely on reliable estimates, stress drop and young modulus have had a secondary effect on the propagation of surface deformation. Secondary to the geological model, which is confirmed to be the key factor in this type of study. Within the numerical modeling it is extremely difficult to consider all the parameters present in the natural system. It is necessary to choose which ones you want to analyze, so you need to establish an order of importance among the possible parameters. The geometry of the fault (dimensions, position, strike, dip, depth) is by far the most important parameter. Still about the geometry of the fault, a third achievement should be mentioned. Knowing the exact geometric parameters of the fault, however important, is difficult in many geological contexts. Regardless of the simulation of the natural case, in this work we were able to reconstruct in 3D a series of non-planar geometries. These two points, 3D and non-planar, add a detail that can increase the accuracy of the result. The use of surface deformation to validate the different tested geometries is a very interesting procedure. The same workflow used, versatile and reliable, can be used in other geological contexts not necessarily for normal faults earthquakes. Although the L'Aquila earthquake is a debated case of study, it foresees the presence of a main fault with a rather simple geometry. In anticipation of future

developments, this same procedure could be applied to the Central Italy 2016 earthquake. The much higher number of mapped coseismic cracks and relocated seismic events would ensure better detail in the interpretation of the geological model. Another potentially interesting case could be the seismic sequence of Emilia 2012. In this case the earthquake was caused by a compressive fault. The presence of numerous wells and seismic lines in the area would help a detailed reconstruction.

Finally, we reconstructed an inversion model in order to observe the slip distribution. This reconstruction was carried out on two distinct geometries in the fusion of the distribution of the surface coseismic deformation. In the absence of direct observations of what was the actual distribution of the slip these reconstructions must be observed with caution. In all two cases the maximum slip and the calculated seismic moment seem to be compatible with the main published reconstructions. However, we can observe two points, the first is that the case with the blind fault seems to show a more coherent result than the case with the outcropping fault. The second point concerns the geometry of the faults and the slip distribution. Normally these inversion models are run on perfectly planar faults. The slip distribution is often concentric with the maximum slip placed in the center of the fault. Using this method instead, the slip is distributed asymmetrically to the fault among separate spots. This distribution, although it cannot be confirmed by direct observation, reiterates the importance of reconstructing a reliable fault geometry. And try to add an element of greater complexity to reconstructions that are often too simplified. The work done during this thesis, thanks to the multidisciplinary approach, helped to clarify different aspects related to the natural study case. At the same time, however, he helped develop procedures and know-how applicable for further studies in different geological contexts.





## Acknowledgments

At the end of this thesis, I would like to thank my supervisors.

Professor Michele Cooke and all the people of the Department of Geosciences of UMass at Amherst, who welcomed me for 9 months.

I would also like to thank the “Bando mobilità internazionale” of the University of Pavia, which helped me support part of the experience in the United States.

Thanks to my colleagues; Niccolò, Riccardo, Silvia, Emanuele, Joan, Roberta, Camilla, Chiara, Mattia, Alberto et al.

Thanks to the Umass Guys; Marsha, Evan, Laura, Jenn, Karin, et al.

Thanks to my family and my friends, I would do very little without them